NEOCLASSICAL CURRENTS IN THE

WISCONSIN LEVITATED OCTUPOLE

by

STEPHEN VINCENT PAINCHAUD

A thesis submitted in partial fulfilment of the requirements for the degree of

Doctor of Philosophy
(Physics)

at the

UNIVERSITY OF WISCONSIN - MADISON

1987

Contents

Chapter 1

Introduction

In a magnetically confined toroidal plasma, collisional transport leads to particle diffusion and heat conduction across magnetic flux surfaces, and current flow along magnetic field lines. A magnetic flux surface is defined by following a field line around the torus as it ergodically covers the surface. Figure 1-1 shows a typical flux surface and several loops of the enveloping field line.

Classical transport theory derives transport coefficients based on the random walk of particles across field lines as they undergo coulomb collisions that shift the center of their gyro-orbits. This theory is valid when the drifts of particles perpendicular to a flux surface is negligible. For a magnetized plasma, where the the particle collision frequency is much less than its gyrofrequency, the step size of this random walk is the particle gyroradius. For diffusion perpendicular to the magnetic flux surfaces the classical particle diffusion coefficient will then have the dependence $D_\perp \sim \nu\rho^2$, where ν is the particle collision frequency and ρ is the particle gyroradius.

In the neoclassical transport theory[1][2] the drift orbits of particles across magnetic surfaces are considered in the diffusion process. If the plasma is relatively collisionless, such that the mean free path for 90° scattering is on the order of the plasma major radius, or larger, then a particle's guiding center can drift significantly from its original flux surface before undergoing a collision. The increase in magnetic field towards the major axis of a toroidally confined plasma can then trap many particles in what is in effect a magnetic mirror. These particles will then describe *banana* orbits as they bounce between turning points with a frequency $\omega_b \geq \nu$. Particles that are untrapped have a pitch angle small enough to allow them poloidally traverse the plasma. Figure 1-2 illustrates a poloidal cross section of several possible particle orbits. The two well-trapped orbits are for particles whose velocities parallel to the magnetic field are of the same magnitude, but oppositely directed.

For both trapped and untrapped particles the effective step size for diffusion is the distance a particle drifts perpendicular to a flux surface during an

orbit. For trapped particles this distance is the width of its banana orbit. For an untrapped particle it is the distance it traverses across flux surfaces as it moves from the outside to the inside of the torus. In both cases this distance is greater than a gyroradius.

The effective collision frequency for trapped particles is the frequency for scattering to an untrapped orbit, given by $\nu_{eff} = (B/\Delta B)\nu$ [2], where ΔB is the field variation along the banana orbit. When $\nu_{eff} < \omega_b$ the trapped particle can complete their banana orbits. The dominant cotribution to the diffusion will then come from the trapped particles since their guiding centers make the largest radial excursions. The overall effect of the drift orbits is to enhance perpendicular diffusion over the predictions of classical theory.

The collisionless regime is also called the banana regime, after the shape of the trapped particle orbits. If the effective collision frequency is comparable to the bounce frequency ω_b, then the plasma is in the plateau regime, which is a transition between the banana regime and the collisional Pfirsch-Schlüter regime. In the Pfirsch-Schlüter regime we have $\nu \gg \omega_b$.

Neoclassical transport theory predicts the existence of *bootstrap* current[3][4] in collisionless plasmas with a significant population of trapped particles. This unidirectional current flows along field lines, and is generated by the balanc-

ing of ion-electron friction forces with the viscous forces between trapped and untrapped like particles. The current is driven by gradients in the plasma pressure and temperature. The other components of the parallel current are the Pfirsch-Schlüter current and any ohmically driven currents. The Pfirsch-Schlüter current is the the current necessary to ensure charge neutrality in the presence of diamagnetic currents.

An Onsager matrix[5] relates the current parallel to the field lines and the particle and heat fluxes perpendicular to the magnetic surfaces to the thermodynamic forces that drive them.

$$\begin{pmatrix} \Gamma_\perp \\ Q_\perp \\ j_\parallel \end{pmatrix} = \begin{pmatrix} L_{11} & L_{12} & L_{13} \\ L_{21} & L_{22} & L_{23} \\ L_{31} & L_{32} & L_{33} \end{pmatrix} \begin{pmatrix} -\nabla_\perp p \\ -\nabla_\perp T \\ E_\parallel \end{pmatrix}$$

The quantities $\Gamma_\perp$ and $Q_\perp$ are the perpendicular particle and heat flux, and $j_\parallel$ is the parallel current density. The driving forces are the perpendicular pressure and temperature gradients, $\nabla_\perp p$ and $\nabla_\perp T$, and the parallel electric field, $E_\parallel$. The diagonal matrix elements are just the diffusion and heat conduction coefficients and the electrical conductivity. The off diagonal elements of this Onsager matrix are interrelated by various symmetries[5].

Past experiments have usually been inconclusive as to the existence of the bootstrap current. Measurements taken on Proto-Cleo[6] in the early 1970's failed to find the diffusion driven bootstrap current as predicted for stellarators. Experiments on the L-1 and Uragan stellarators[7][8] found parallel currents differing from the neoclassical theory and postulated this disparity was due to effects of rf heating[7] or radial electric fields[8]. Results from the ISX-B tokamak experiment[9] report that the bootstrap current can be at most 25% of the predicted value. More recent experiments on Proto-Cleo at Wisconsin[10] found that the measured neoclassical current agreed well with theory, except for in a small region near the magnetic axis. Unfortunately the Wisconsin Proto-Cleo experiment used axisymmetric theory for a nonaxisymmetric device (stellarstor), and included the theoretical effects of a toroidal rotation of plasma with no proof that such a rotation existed. A nonaxisymmetric theory, with no toroidal rotation of the plasma, would have predicted much lower values of the parallel current. Recent results from TFTR[11] indicate the existence of non-ohmically driven current, though the mechanism that generates this current has yet to be determined.

Previous work by M.C. Zarnstorff[12][13][14] has identified the existence of bootstrap current in the Wisconsin Levitated Octupole. Both the total

parallel current and the ion contribution to $j_{\|}$ were separately measured. The total $j_{\|}$ was found to adhere to predicted values on some flux surfaces and have significant variation from theory on other surfaces. The ion portion of $j_{\|}$ was in good agreement with theory in the common flux region, but not measured in the private flux region.

The discovery of bootstrap current in the Octupole naturally leads to the question of why previous experiments were unsuccessful in their endeavors to identify this current. The original motivation for this thesis was to address that question, by investigating the effects on bootstrap current caused by ohmic currents, plasma fluctuations, and rf fields. Ohmic currents, while naturally present in tokamaks, can be introduced in the Octupole, independent of the usual operating procedure, and can be adjusted to be of the same order of magnitude as the expected diamagnetic and parallel currents. The interaction, if any, of bootstrap current and ohmic current can thus be determined without the problem of a large ohmic current masking the neoclassical current. RF fields can be driven in the Octupole plasma with little or no plasma heating. Any anomalous effects on the parallel currents, due to the existence of the rf fields, can then be determined. Fluctuation level differences, in the private and common flux regions (described in chapter 2), allow the effect of the

fluctuations on parallel currents to be discerned.

This thesis reports results differing from previous observations[12], in that little agreement is found between the experimentally measured total parallel current and the theoretically expected current. This dichotomy, between theory and experiment, might possibly be explained by documented magnetic field errors in both the toroidal and poloidal fields of the Octupole. These field errors would lead to the trapping of particles by local maxima of the field perturbation[2], which would result in parallel currents differing from those predicted for an axisymmetric plasma. Since the exact nature of field errors in the Octupole are unknown, no other mention of this line of inquiry will be made.

This thesis consists of four parts: Chapter 2 describes the experimental apparatus and the plasma diagnostics used in these studies. Chapter 3 delves into the general theory of neoclassical currents (excluding field errors) and how it is applied to the Octupole. Chapter 4 explains the experimental results of this investigation. Chapter 5 gives a brief discussion of the conclusions that can be inferred from the data.

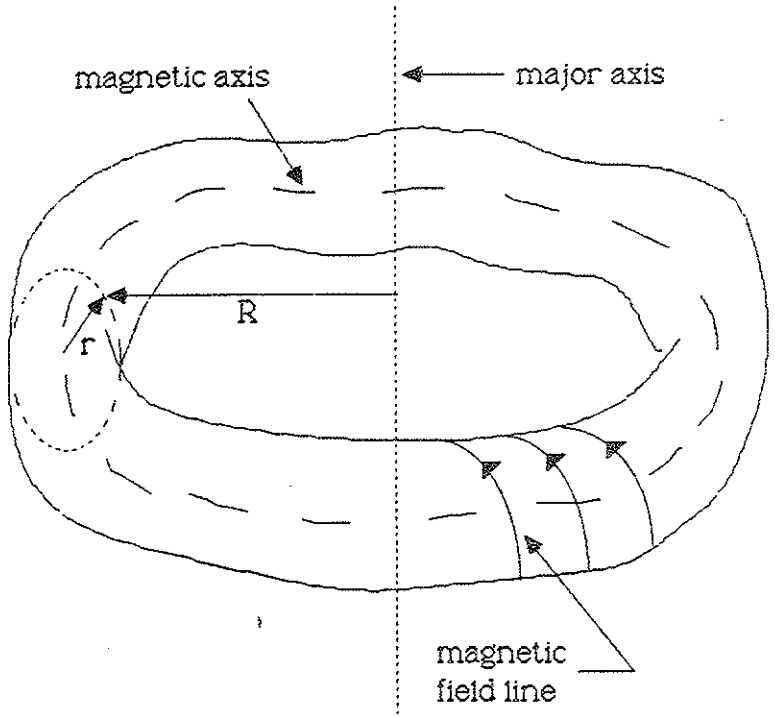

Fig. 1-1. A toroidal flux surface defined by the magnetic field line that ergodically covers it. On a magnetic surface where the safety factor, $q = r B_T / R B_p$, is a rational number, the field line will close upon itself.

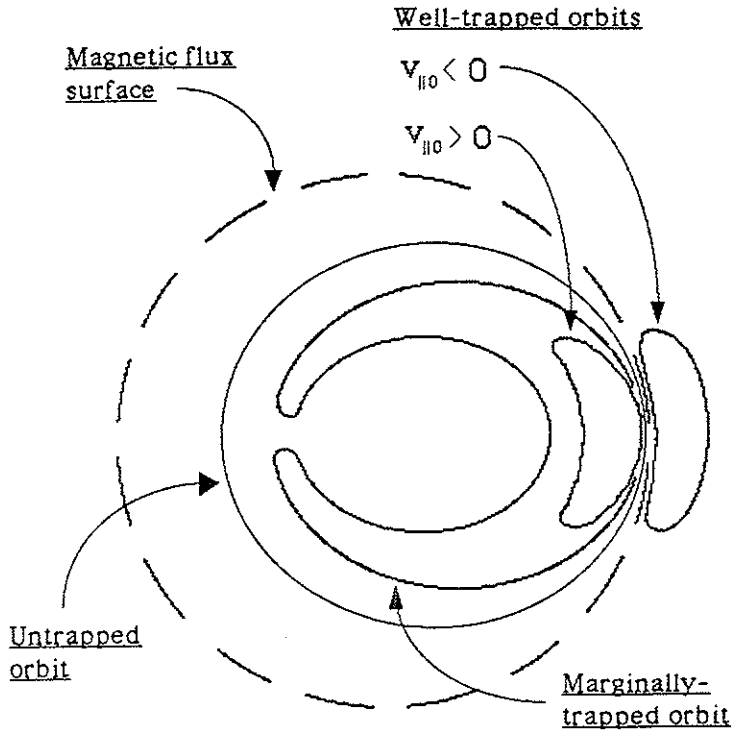

Fig. 1-2 Guiding center orbits of trapped and untrapped particles, projected on a plane of constant toroidal angle, in an axisymmetric system.

Chapter 2

Experimental Apparatus

This chapter describes the experimental apparatus, plasma diagnostics and diagnostic methods used for this work. Most of the experiments were done using the Wisconsin Levitated Octupole. As of Febuary 1985 the Levitated Octupole program was phased out to enable experimentation on reversed field pinch plasmas. Some investigations were done on the Wisconsin Tokapole II, however it was found to be inadequate for this work.

2.1 The Wisconsin Levitated Octupole

The Wisconsin Levitated Octupole, shown in Fig. 2-1, is a large axisymmetric toroidal plasma device. Some of the Octupole parameters are listed in Table 2-1.

The poloidal cross section is roughly square, with *noses* (Fig. 2-2) projecting in horizontally at the midcylinder. Within the Octupole are four current carrying aluminum rings. The magnetic fields are admitted through insulated poloidal and toroidal gaps in the aluminum vacuum vessel. The poloidal field is created with an iron core transformer threaded through the Octupole, which inductively drives toroidal current in the walls and internal rings. Current can flow toroidally in the wall, across the poloidal gap, through the use of continuity windings that bridge the gap and circle around the outside of the transformer. The toroidal field is created by driving poloidal current in the vacuum vessel, with a half-sine period slightly less than that of the poloidal field.

The poloidal flux plot is essentially that of an octopole field, as shown in Fig. 2-2. There are three field nulls strung vertically along the midcylinder. Most of the flux either encircles a single ring, and is called private flux, or is

Table 2-1

Octupole Parameters

Major radius	1.4 m
Minor cross section	1.12 m × 1.2 m
Hoop minor radius	8.89 cm
Hoop major radius: inner	1.0 m
outer	1.8 m
Vacuum volume	8.6 m^3
Poloidal field half-sine period	43 msec
Poloidal field capacitor bank	.048 F
Maximum energy pulse	0.6 MJ
Maximum core flux	0.72 Wb
Maximum hoop current: inner	0.46 MA
outer	0.25 MA
Maximum toroidal wall current	1.40 MA
Maximum B_p at hoop: inner	13.7 kG
outer	6.6 kG

common flux and encircles all four rings. A small amount of flux is common to only two rings. The private and common flux regions are separated by a flux surface designated as the separatrix.

The poloidal flux surfaces in the Octupole are designated in units from zero to ten, where the surface $\psi = 0$ is in the ring and the surface $\psi = 10$ is in the wall. A unit of flux is therefore equal to $^1/_{10}$ of the total poloidal flux in the Octupole. During the pulse the position of these flux surfaces shift as the poloidal magnetic field soaks into the rings and walls. The stable plasma region, i.e. good curvature region, is inside the separatrix at $\psi_{sep} = 5.7$, designated in Fig. 2-2 by a dashed curve. Between the separatrix and $\psi_{crit} = 8.1$ the plasma is average minimum B stable. Outside of this *critical* flux surface the plasma is MHD unstable. The dot-dash curve in Fig. 2-2 is ψ_{crit}. The psi values given above are for a time at the peak of the poloidal field, about 20 msecs into the field pulse.

The rings are supported by prods that can be quickly retracted from the flux region, then reinserted to catch the rings as they begin to fall. This allows the rings to *levitate* during the experiment, so that they are isolated from the vessel walls, and keeps the prods from cutting across flux surfaces.

The base vacuum of the Octupole is about 10^{-8} torr. This vacuum is

achieved with two turbo pumps, six titanium getters, and a cryogenic panel. The cryogenic panel can be valved off from the main tank so that the gases it pumps are not dumped back into the toroid when the panel is heated.

Diagnostic probes can access the plasma through quarter inch probe ports. The ports are spaced 90 degrees apart toroidally and about 15 to 30 degrees apart in the poloidal direction. The poloidal direction has 270 degrees of probe port access, the wall near the central axis being excluded.

2.2 Plasma Generation

Plasma is created with the *intermediate* Marshall gun [15], and injected into the Octupole. The gun's 60 μF capacitor bank was charged to 14 kV, the gas plenum filled to 50 psig with H_2, and the valve-to-gun timing was 400 μsec. The poloidal and toroidal fields were triggered to peak concurrently, to minimize time dependence of the field line pitch. Plasma was injected near the peak of the field pulse to avoid having any current driven by the induced electric fields.

The intermediate gun provided plasma consistent with the assumptions of neoclassical theory, i.e., the ion gyroradius ($\sim$ .5 cm) is small compared

Table 2-2

Typical Plasma Parameters

@ 400μsec

$n_e \sim 8 \times 10^{12}$ cm^{-3}
$T_e \sim T_i \sim 20eV$
$\beta \sim 2\%$
$\tau_\beta \sim$ 1 msec, beta decay on separatrix
$\rho_i \leq .5cm$ on separatrix
$B_p \sim$ 860G on separatrix
$B_t \sim$ 200G on separatrix

to typical gradient scale lengths ($\geq$ 1.0 cm), and the collision frequency ($\leq 2 \times 10^8\ sec^{-1}$) is small compared to the gyrofrequency ($\sim 3 \times 10^9\ sec^{-1}$). Plasma β was high enough to give measurable plasma current signals without undue distortion of the flux surfaces, yet the density was low enough for the plasma to exist in the banana regime ($\lambda_{ee} \sim$ 2.0 meters). Typical plasma parameters are listed in Table 2-2.

2.3 Driving Ohmic Currents

Ohmic currents were driven in the Octupole plasma by discharging a small capacitor bank, of about 480μF, across the poloidal gap, at the peak of the main fields. The secondary poloidal field this creates is on the order of 3–5% of the main field, at a frequency of 300Hz. The polarity of this secondary field is determined by the choice of the capacitor bank used. Figure 2-3 shows the circuit used to drive the ohmic currents. The Octupole is represented by its time dependent resistance and inductance, R_p and L_p. The choice of the "positive" or "negative" ohmic current bank determines the secondary field polarity with respect to the main poloidal field.

The currents that were driven are on the order of 0.5–1.0 A/cm^2, which is about the same magnitude as the diamagnetic and parallel currents in a typical plasma without ohmic current.

2.4 General Plasma Diagnostics

2.4.1 Plasma Density - n

The plasma electron density is measured with a 70 GHz microwave interferometer. The microwave beam travels a vertical path through the Octupole's midcylinder. The interferometer actually measures $\int n_e dl$, but to within a few percent this directly gives the separatrix density, since the flux surfaces along the beam path are dominated by the separatrix region of flux space (Fig 2-2).

Langmuir floating double probes are used to measure the density profile. These probes consist of .04 inch diameter platinum spheres about 2–3 millimeters apart. The typical bias between the spheres was about 100 V. The measured ion saturation current should vary as

$$I_s \sim n_i \sqrt{T}$$

where T is the greater of T_e or T_i. For our experiments we have found that $T_e \simeq T_i$, therefore T_e is used to unfold the density profile. The proportionality constant is determined by setting the density on the separatrix equal to the density given by the interferometer.

2.4.2 Electron Temperature

The temperature of the electrons is determined using an admittance probe technique developed by J.C. Sprott [16]. A third platinum tip is added to a floating double probe, in order to measure plasma sheath impedance, R_s. This third tip, identical to the other two tips, is connected to a 400 kHz capacitive bridge circuit. The electron temperature (in eV) is then given by

$$T_e = eI_sR_s.$$

If the areas of the probe tip measuring sheath impedance and the tip collecting ions are not identical, then the above expression is modified by the ratio of the areas.

From the capacitive bridge, the admittance signal is demodulated using the active full-wave rectifier shown in Fig. 2-4. The digitally recorded signal is then compared to a calibration curve to give the value R_s. The ion saturation current and sheath impedance together give T_e vs time at the probe tip.

2.4.3 Ion Temperature

The ion temperature in a typical Octupole plasma, has been measured in past experiments[17] with electrostatic gridded energy analyzers. It has been

found, for the types of plasmas created in this experiment, that $T_e \simeq T_i$. This is a reasonable approximation since, for plasma of interest, the thermal equilibration time is $\tau_e^{e/i} \leq 500\mu$sec, while the temperature decays on a 1.0–1.5 msec time scale.

2.5 Plasma Current Diagnostics

2.5.1 General Method

The total plasma current density in the Octupole was measured using a multi-coil magnetic probe, hereafter referred to as a $\dot{B}$ probe, with two parallel coils displaced by about 1cm along the probe. The probe was generally used with the coils displaced perpendicular to a flux surface. The signal from the first coil and the difference signal from the two coils can be integrated to give measurements of the magnetic field and its gradient perpendicular to the flux surface. The integrated signals are then digitized and recorded to magnetic disk. The difference between the vacuum magnetic field measurements and measurements of a shot with plasma then gives the magnetic field (δB) and field gradient ($\delta \nabla B$), where the δ denotes a change in a quantity due to the plasma currents. The subtraction of the vacuum pulse from the plasma shot

is done by computer. As shown in the next section, these signals can then be used to determine the plasma current density.

The integrators are turned on about 300μsec after the Marshall gun fires to avoid noise due to the gun firing. At this time the plasma in the Octupole is axisymmetric. Since the $\partial_t B$ and $\partial_t \nabla B$ (where ∂_t denotes the time derivative) are small at this time these gated integrators have been made very sensitive so that small changes in the magnetic field can be measured.

On a given field pulse the $\dot{B}$ probe is aligned to measure either the toroidal or poloidal field, thus allowing calculation of either the poloidal or toroidal current, respectively. In order to construct the parallel and perpendicular components of $\vec{j}$ it is necessary to use currents calculated from two shots with different probe orientations. This is done by first matching plasmas that have similar characteristics, both in magnitude and time decay. The characteristics chosen for the matching were electron beta β_e, and λ_{ee}, the mean free path for electron on electron collisions. In principle these two characteristics determine the magnitude of δB and the collisionality regime of the plasma, respectively. The current densities, j_p and j_t, from matched pairs of shots are then used to construct $j_\perp$ and $j_\parallel$.

In order to avoid the problems inherent with finding matched pairs of shot,

measurements were taken using a probe with a second set of coils orthogonal to, and wound concentric with the first set. Capacitive coupling between concentric coils produced unreasonable results. Although it is probably possible to electrostatically shield the coils from each other the attempt was not made.

2.5.2 Calculation of Currents

For an axisymmetric toroidal system the components of $\mu\vec{j} = \nabla \times \vec{B}$ give the poloidal and toroidal current densities

$$\mu\vec{j}_p = \partial_\psi B_t + (\hat{\psi} \cdot \hat{R})\frac{B_t}{R}, \tag{2.1}$$

and

$$\mu\vec{j}_t = -\partial_\psi B_p + (\hat{\psi} \cdot \vec{\kappa}_p)B_p, \tag{2.2}$$

where $\vec{\kappa}_p = \hat{\chi} \cdot \nabla\hat{\chi}$ is the poloidal field curvature, $\hat{\chi}$ is the unit vector in the poloidal direction, and $\hat{\psi}$ is the unit vector normal to the flux surface.

At the poloidal angle where measurements for this experiment were taken $\hat{\psi} \cdot \hat{R} = 1$ and $\hat{\psi} \cdot \vec{\kappa}_p = -\mid \vec{\kappa}_p \mid \equiv -\kappa_p$. The current density equations then simplify to

$$\mu\vec{j}_p = \partial_\psi B_t + \frac{B_t}{R}, \tag{2.3}$$

and

$$\mu\vec{j}_t = -\partial_\psi B_p - \kappa_p B_p. \tag{2.4}$$

From equation 2.4 we can see that the field curvature can be calculated from a vacuum field shot, where $j_t = 0$, to obtain

$$\kappa_p = -\frac{\partial_\psi B_p}{B_p}.$$

2.5.3 Field Coils

The coils used to measure the magnetic fields where wound on a machined G10 coil form shown in Fig. 2-5. Each coil was wound with about 110 turns of #42 copper magnet wire, and had a cross section of 2.5mm × 5.0mm. The separation between the coil centers was 1cm. The coils were electrostatically shielded with 13 μm-thick aluminum foil. The coils are electrically insulated from the plasma by inserting them in a 1/4 inch O.D. pyrex tube.

2.5.4 Active Integrators

The circuitry for the front end amplifiers to the active integrators is shown in Fig. 2-6. The differential and single-ended inputs are used to measure $\nabla_\psi B$ and B respectively.

The schematic for the gated and non-gated integrators is shown in Fig. 2-7. The non-gated integrator was used to obtain the background magnetic fields and field gradients. The gated integrator was used to discern the magnetic fields created by the plasma currents.

Both the field coils and the active integrators were developed by M.C. Zarnstorff and are described in more detail in his thesis[12].

2.5.5 Data Aquisition

At each orientation of the magnetic probe two vacuum field shots were taken to form a baseline to subtract from subsequent shots with plasma. The integrators are usually stable enough that baseline drift over the time of the experiment is insignificant.

Each set of integrators, as shown in Fig. 2-7, is calibrated with respect to the lowest gain of the gated integrator. The calibration is stored with each data shot. The overall difference in the gains of the two sets of integrators is taken into account when calculating the currents as described in section 2.5.2.

The signals from all diagnostics are sent to Lecroy model 8210 A-D converters and sampled at a rate of 100kHz(25kHz for the nongated magnetic probe). The digitized signals are stored on magnetic disk along with diagnostic dependent information on scale factors, sampling rates, etc.

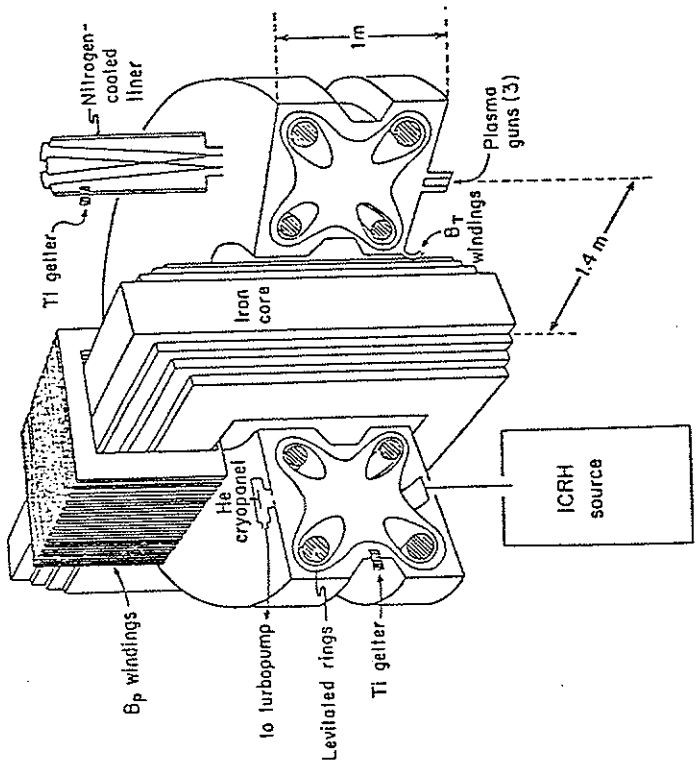

Fig. 2-1. Wisconsin Levitated Octupole

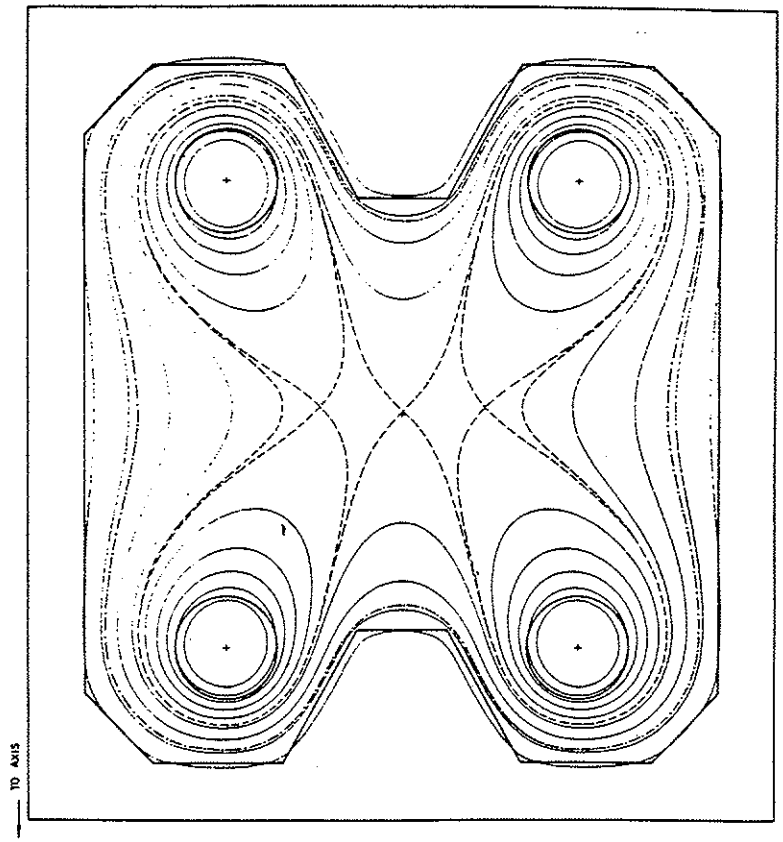

Fig. 2-2. Poloidal flux plot of the Octupole.

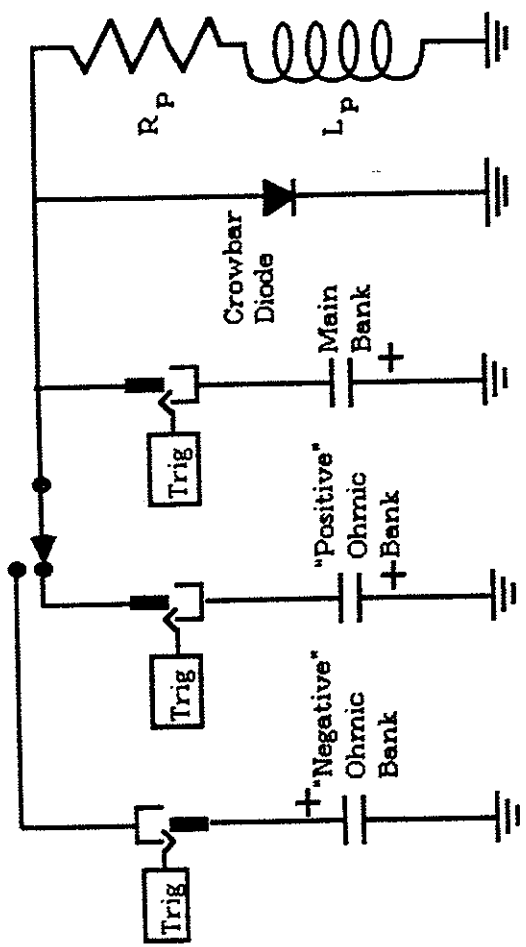

Fig. 2-3. Schematic diagram of Octupole circuit. R_p and L_p are the resistance and inductance of the Octupole poloidal field windings.

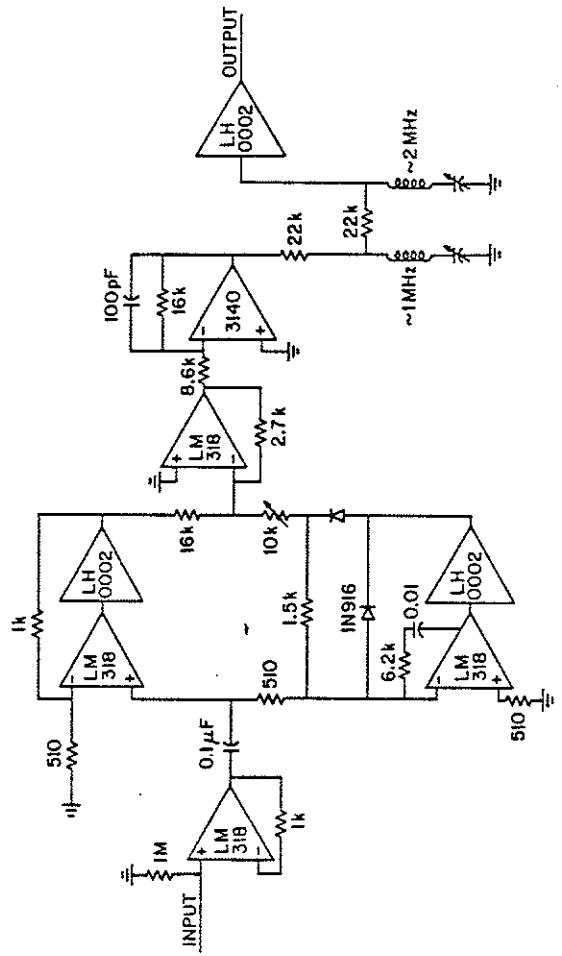

Fig. 2-4. Rectifier circuit used to demodulate the signal from the admittance bridge.

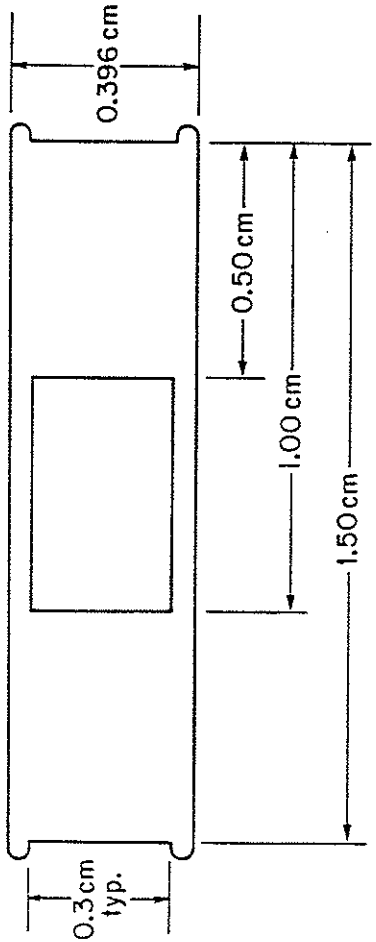

Fig. 2-5. Coil form used for two-coil magnetic probe.

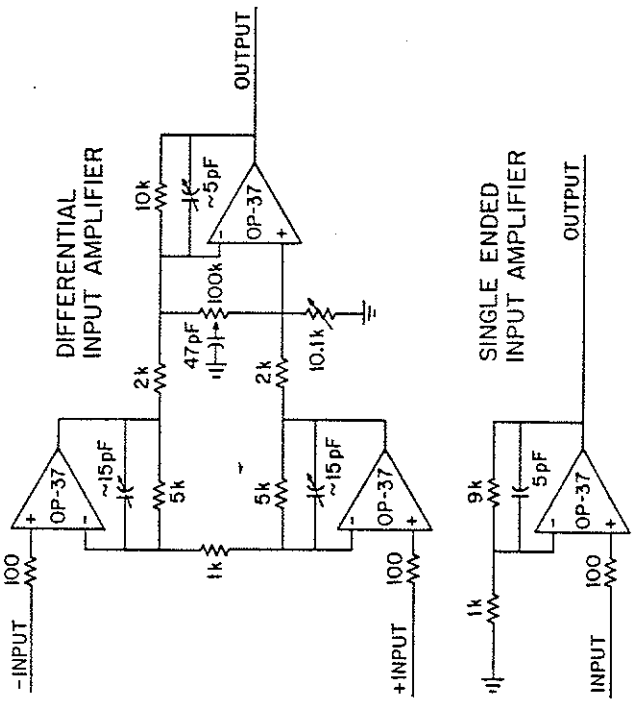

Fig. 2-6. Front-end amplifiers for the magnetic probe. The amplifier with the single input is used for measurements of B. The differential amplifier is used to measure the gradient of B.

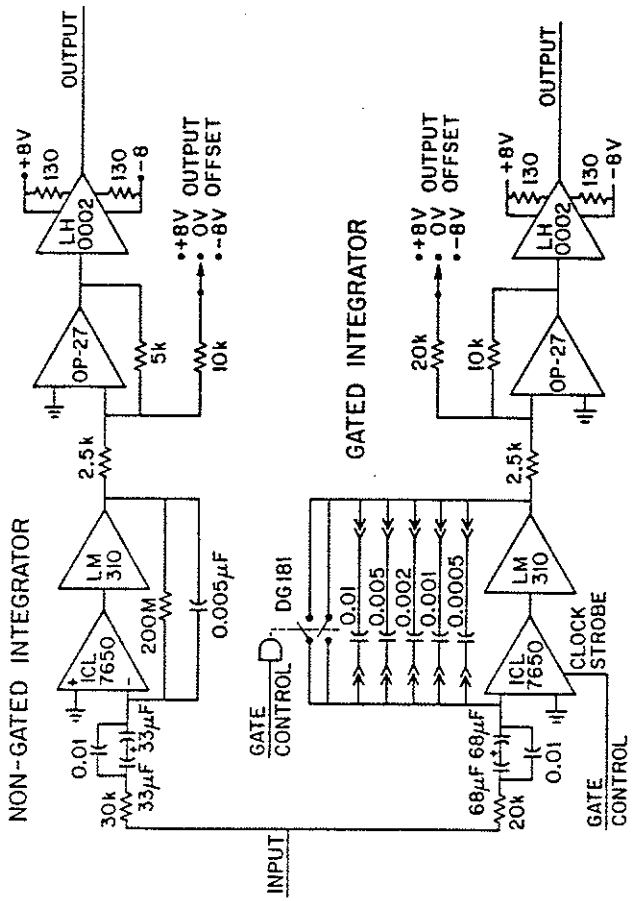

Fig. 2-7. Integrating amplifiers for the magnetic probe.

Chapter 3

Theory of Neoclassical Currents

The kinetic theory of plasma transport in tokamaks was initiated in 1968 by Galeev and Sagdeev[1]. They demonstrated that the banana orbits of trapped particles were responsible for an enhancement of the calculated diffusion coefficient and thermal conductivity in a plasma with a small collision frequency. The existence of the intermediate plateau regime was also shown.

In 1971 the existence of the bootstrap current was predicted independently by Galeev[3] and by Bickerton, Connor, and Taylor[4]. The latter authors predicted that the bootstrap could provide the confining poloidal magnetic field in a steady-state tokamak without the need of driving ohmic currents. In 1976 Hinton and Hazeltine[2] summarized the kinetic theory of plasma transport in

a review of the theory to that date. At this point the theory only dealt with large aspect ratio configurations with circular and elliptical flux surfaces. In 1981 the moment equation approach of Hirshman and Sigmar[5] allowed the calculations of neoclassical transport and currents for axisymmetric geometries with arbitrary cross section.

Throughout these years there has evolved an extensive body of literature dealing with neoclassical transport and related effects. All the authors of theorectical papers referenced in this thesis have made contributions to the theory that could easily expand my references by an order of magnitude. Many other authors have also made immense contributions to the theory, too many to mention in this thesis. A more complete list of references can be found in the review papers by Hinton and Hazeltine[2] and by Hirshman and Sigmar[5].

The theory presented in this chapter was chiefly derived from review papers written by Hinton and Hazeltine[2] and by Hirshman and Sigmar[5]. It is presented here, in condensed form, since it is necessary to understand the theory in order to apply it to the Octupole. All the theory presented in this thesis is readily found in the existing literature, and the application to the Octupole was developed by M.C. Zarnstorff[12].

3.1 Structure of the Equilibrium Currents

The total current in a magnetized plasma can be written as

$$\vec{j} = \vec{j}_\perp + j_\parallel \frac{\vec{B}}{B}. \tag{3.1}$$

To first order in the Larmor radius expansion the diamagnetic current is given by

$$\vec{j}_\perp = \frac{\vec{B} \times \nabla p}{B^2}, \tag{3.2}$$

and the parallel current is defined by

$$j_\parallel = \frac{\vec{j} \cdot \vec{B}}{B}.$$

Using flux coordinates, for an axisymmetric torus, the magnetic field equations can be written as

$$\vec{B} = \vec{B}_p + \vec{B}_t$$

$$\vec{B}_p = \nabla\psi \times \nabla\phi$$

$$\vec{B}_t = F(\psi)\nabla\phi$$

where ψ is the poloidal flux, ϕ is the toroidal angle, the poloidal angle is defined by $\hat{\chi} = \hat{\psi} \times \hat{\phi}$ and $F(\psi) = RB_t$. The magnitude of the diamagnetic current can be simplified to

$$j_\perp = Rp' \frac{B_p}{B} \tag{3.3}$$

where the prime denotes ∂_ψ. Eq. 3.2 is true for an axisymmetric toroidal system with closed magnetic flux surfaces, since the plasma pressure will then be a flux surface constant.

The poloidal component of Eq. 3.1 can be solved for $j_\parallel$ to yield

$$j_\parallel = \frac{Fp'}{B} + KB \tag{3.4}$$

where

$$K = \frac{\vec{j} \cdot \vec{B}_p}{B_p^2} = \frac{j_p}{B_p}$$

is proportional to the poloidal current. The equilibrium continuity equation gives

$$\nabla \cdot \vec{j} = \partial_\chi (j_p / B_p) = 0,$$

from which follows the observation that $K = K(\psi)$ is constant on a flux surface.

The first term on the right side of Eq. 3.4 is the parallel current necessary to cancel charge accumulation due to the diamagnetic current. The second term is a divergence-free current (note $\nabla \cdot K\vec{B} = 0$) that is determined by the equilibrium moment balance along $\vec{B}$.

If we multiply Eq. 3.4 by $|B|$ and average over a flux surface we get

$$K(\psi) = \frac{\langle \vec{j} \cdot \vec{B} \rangle}{\langle B^2 \rangle} - \frac{Fp'}{\langle B^2 \rangle}, \tag{3.5}$$

where the flux surface average is defined by

$$\langle A \rangle \equiv \frac{\oint A dl_\parallel / B}{\oint dl_\parallel / B}.$$

Combining Eqs. 3.4 and 3.5 we have

$$j_\parallel = \frac{Fp'}{B}\Big(1 - \frac{B^2}{\langle B^2 \rangle}\Big) + \frac{\langle \vec{j} \cdot \vec{B} \rangle}{\langle B^2 \rangle} B. \tag{3.6}$$

The first term in Eq. 3.6 is the Pfirsch-Schlüter current

$$j_{PS} = \frac{Fp'}{B}\Big(1 - \frac{B^2}{\langle B^2 \rangle}\Big).$$

Note that $\langle j_{PS} \rangle = 0$, and that j_{PS} reverses sign at the point along a field line where $B^2 = \langle B^2 \rangle$.

The second term in Eq. 3.6 contains the neoclassical current and ohmically driven current. The ohmic current can be expressed as

$$j_B = \sigma_{NC} \frac{\langle \vec{E} \cdot \vec{B} \rangle}{\langle B^2 \rangle} B,$$

where σ_{NC} is the neoclassical plasma conductivity.

The bootstrap current

$$j_B = \frac{\langle \vec{j} \cdot \vec{B} \rangle}{\langle B^2 \rangle} B - j_B,$$

is a current driven by pressure and temperature gradients in the plasma. It is a divergence-free current and, unlike j_{PS}, it is unidirectional on any flux surface where $B \neq 0$. In the next section it will be shown that the bootstrap current is generated by the viscous force between trapped and circulating particles (Fig 3-2), and that the bootstrap current is small in the collisional regime, and dominates j_{PS} in the banana regime. A theoretical calculation of both the bootstrap current and the neoclassical plasma conductivity will be presented below.

3.2 Detailed Calculation of the Currents

3.2.1 General Method

The detailed calculation of the neoclassical current requires that we solve for the fluid flows $\vec{u}_a$ to obtain the parallel current density $j_{\|} = en(u_{i\|} - u_{e\|})$. Starting with the plasma fluid equations, from which we can obtain parallel moment balance equations relating the parallel viscous and frictional forces. The parallel frictional forces can be shown to be related to the parallel fluid velocity $u_{\|}$ and heat flux $q_{\|}$ through the friction coefficients. The parallel viscous forces are related to the poloidal flows $\vec{u}\cdot\vec{B}_p/B_p$ and $\vec{q}\cdot\vec{B}_p/B_p$ through the viscosity coefficients. At this point the fluid velocity for each species can be found in terms of viscosity and friction coefficients and basic plasma parameters.

The second part of the problem is to find expressions for the viscosity and friction coefficients. The friction coefficients are found to be independent of the collisionality regime of the plasma. Starting with the drift-kinetic equation, the viscosity coefficients can be approximated for the various collisionality regimes, and these expressions are then smoothed to form expressions valid over all regimes. Fig. 3-1 shows a flow diagram outlining the steps in the

derivation.

3.2.2 Fluid Equations

The distribution function, $f_a(\vec{x},\vec{v},t)$, of particles of species a, with charge e_a, and mass m_a, satisfies the Fokker-Planck equation,

$$\frac{\partial f_a}{\partial t} + \vec{v}\cdot\nabla f_a + (e_a/m_a)(\vec{E}+\vec{v}\times\vec{B})\cdot\frac{\partial f_a}{\partial \vec{v}} = C_a(f_a) \tag{3.7}$$

where $\vec{E}$ and $\vec{B}$ are, respectively, the macroscopic electric and magnetic fields, and C_a is the Fokker-Planck collision operator:

$$C_a = \sum_b C_{ab},$$

$$C_{ab} = -\frac{2\pi e_a^2 e_b^2}{m_a}\ln\Lambda\frac{\partial}{\partial v_\alpha}\int d^3v'\left[\frac{f_a(\vec{v})}{m_b}\frac{\partial f_b(\vec{v}')}{\partial v'_\beta} - \frac{f_b(\vec{v}')}{m_a}\frac{\partial f_a(\vec{v})}{\partial v_\beta}\right]U_{\alpha\beta}(\vec{v}-\vec{v}'),$$

$$U_{\alpha\beta}(\vec{x}) \equiv x^{-3}(x^2\delta_{\alpha\beta} - x_\alpha x_\beta),$$

where the summation is over all particle species b, and a sum over the repeated Cartesian indices (α,β) is implied.

The velocity moments of the Fokker-Planck equation give the plasma fluid equations. For convenience, the species subscript will be omitted in the following equations. The expressions for particle and energy conservation, obtained from the $|v|^0$ and v^2 moments, respectively, may be written as

$$\frac{\partial n}{\partial t} + \nabla\cdot(n\vec{u}) = 0, \tag{3.8}$$

$$\frac{\partial}{\partial t}\left(\frac{3p}{2}\right) + \nabla\cdot\vec{Q} = Q + \vec{u}\cdot(\vec{F}+en\vec{E}), \tag{3.9}$$

where Eq. 3.8 is valid for small $\vec{u}$. The expressions for the conservation of momentum and of energy flux, obtained from the $\vec{v}$ and $v^2\vec{v}$ moments, respectively, are written as

$$\frac{\partial}{\partial t}mn\vec{u} + \nabla\cdot\mathbf{P} - en(\vec{E}+\vec{u}\times\vec{B}) = \vec{F}, \tag{3.10}$$

$$\frac{\partial}{\partial t}\vec{Q} + \nabla\cdot\mathbf{R} - \frac{3e}{2m}\vec{E}p - \frac{e}{m}\vec{E}\cdot\mathbf{P} - \frac{e}{mc}\vec{Q}\times\vec{B} = \vec{G}. \tag{3.11}$$

The conservation of energy flux is analogous to the conservation of momentum (i.e., particle flux). The change in the heat flux in a fluid volume element, of particle species a, is due to forces on the fluids caused by the macroscopic fields, collisions with other particle species, and the amount of energy flux that leaves or enters the fluid element. For these fluid equations the following quantities are defined:

density : $n = \int d^3v f,$

particle flux : $n\vec{u} = \int d^3v \vec{v} f,$

stress tensor : $\mathbf{P} = \int d^3v m\vec{v}\vec{v} f,$

energy flux : $\vec{Q} = \int d^3v (mv^2/2)\vec{v} f,$

energy weighted stress tensor : $\mathbf{R} = \int d^3v (mv^2/2)\vec{v}\vec{v} f,$

friction force : $\vec{F} = \int d^3v m\vec{v} C(f),$

collisional energy exchange : $Q = \int d^3v (m/2)(\vec{v} - \vec{u})^2 C(f),$

collisional change in energy flux : $\vec{G} = \int d^3v (mv^2/2)\vec{v} C(f),$

and

scalar pressure : $p = nT = \mathbf{Tr}\{\mathbf{P}\}/3,$

where **Tr** denotes the trace.

Another quantity which we define here is the heat flux

$$\vec{q} = \int d^3v (m/2)(\vec{v} - \vec{u})^2 (\vec{v} - \vec{u}) f,$$

which is just the energy flux measured in the reference frame of the plasma.

3.2.3 Small Gyroradius Ordering

The scale length for gradients in thermodynamic quantities, such as the plasma pressure, is given by

$$l = |\nabla ln p|^{-1}$$

the thermal speed is

$$v_T = (2T/m)^{1/2};$$

and the particle transit frequency is given by

$$\omega = v_T/l.$$

The particle gyroradius (Larmor radius) is given by

$$\rho = v_T/\Omega = mv_T/eB.$$

Terms in the fluid equations will be ordered with the assumption of a small gyroradius such that

$$\delta \equiv \rho/l = \omega/\Omega \ll 1.$$

We further assume that the diffusion time scale is such that

$$\partial ln p/\partial t = O(\delta^2 \omega), \tag{3.12}$$

so that the macroscopic plasma parameters are in equilibrium compared to the time scales of other processes. We also assume that $\vec{E} \times \vec{B}$ drift velocities are small compared to the thermal speed,

$$cE/(Bv_T) = O(\delta),$$

so that we can rule out rapid fluid motions associated with the MHD ordering, where $cE/(Bv_T) = O(1)$.

3.2.4 Consequences of the Ordering

It can be shown[2] that that assumption of small gyroradii results in a distribution function that is approximately Maxwellian

$$f = f_M + O(\delta),$$

where

$$f_M = n_0(\pi^{1/2}v_T)^{-3}exp[-(v/v_T)^2].$$

The following terms, which are identically zero when $f = f_M$, must be of first order

$$\{n\vec{u}, \vec{Q}, \vec{F}, \vec{G}, (\mathbf{P} - \mathbf{I}p), [\mathbf{R} - (5pT/2m)]\} = O(\delta), \tag{3.13}$$

where I is the unit dyadic. Conservation of energy in collisions requires

$$\sum_a (Q_a + \vec{F}_a \cdot \vec{u}_a) = 0,$$

from which we see that $Q = O(\delta^2)$, since both both $\vec{F}_a$ and $\vec{u}_a$ are assumed to be $O(\delta)$. Using Eq. 3.13 we see that to lowest order the heat flux can be approximated by

$$\vec{q} = [\vec{Q} - (5/2)p\vec{u}](1 + O(\delta)).$$

Because of the assumed diffusion time scale in Eq. 3.12, the electric field, in a plasma without ohmic currents, must be primarily electrostatic

$$(c/Bv_T)(\vec{E} + \nabla\Phi) = O(\delta^2),$$

where Φ is the electrostatic potential.

By identifying the zero order terms in Eqs. 3.10 and 3.11 we find

$$\vec{B} \cdot [\nabla p + en\nabla\Phi] = O(\delta),$$

$$\vec{B} \cdot [\nabla pT + ep\nabla\Phi] = O(\delta).$$

Together these two equations imply that

$$\vec{B} \cdot \nabla T = O(\delta),$$

$$\vec{B} \cdot \nabla[n\exp(-e\Phi/T)] = O(\delta). \tag{3.14}$$

The quasi-neutrality condition $\sum_a e_a n_a = 0$, combined with Eq. 3.14, then yields

$$\vec{B} \cdot \nabla p = O(\delta),$$

$$\vec{B} \cdot \nabla n = O(\delta),$$

$$\vec{B} \cdot \nabla \Phi = O(\delta).$$

So to lowest order the density, temperature, and electrostatic potential are constant on a flux surface

$$n_a = \overline{n}_a(\psi)[1 + O(\delta)],$$

$$T_a = \overline{T}_a(\psi)[1 + O(\delta)],$$

$$\vec{E} = -\nabla\Phi(\psi)[1 + O(\delta)].$$

3.2.5 Particle and Heat Flux

The perpendicular particle and energy flux can be obtained from Eqs. 3.10 and 3.11, respectively, giving the exact formulae

$$n\vec{u}_\perp = (m\Omega)^{-1}\hat{n} \times [\nabla \cdot \mathbf{P} - \vec{F} - en\vec{E} + \partial_t(mn\vec{u})],$$

$$\vec{Q}_\perp = \Omega^{-1}\hat{n} \times [\nabla \cdot \mathbf{R} - \vec{G} - (e/m)\vec{E} \cdot (\mathbf{P} + (3/2)p\mathbf{I}) + \partial_t\vec{Q}],$$

where $\hat{n} = \vec{B}/B$. Notice that to find the flows through $O(\delta^n)$ is is only necessary to evaluate the expressions in the brackets above through $O(\delta^{n-1})$.

To lowest order the equilibrium perpendicular flows are

$$n\vec{u}_\perp = (m\Omega)^{-1}\hat{n} \times (\nabla\overline{p} + e\overline{n}\nabla\Phi),$$

$$\vec{Q}_\perp = \Omega^{-1}\hat{n} \times [(5/2m)\nabla\overline{pT} - (5e/2m)\vec{E}\overline{p}]$$

$$\vec{q}_\perp = (5/2)(m\Omega)^{-1}\overline{p}\hat{n} \times \nabla\overline{T}.$$

These flows obviously remain in a magnetic surface since

$$n\vec{u}_\perp \cdot \nabla\psi = \vec{q}_\perp \cdot \nabla\psi = 0.$$

In equilibrium, the lowest order terms of Eqs. 3.8 and 3.9 give

$$\nabla \cdot n\vec{u} = \nabla \cdot \vec{Q} = \nabla \cdot \vec{q} = 0.$$

which can be combined with the formulas for the perpendicular flows, and integrated to find the parallel particle and heat flux

$$nu_\parallel = nu_\vartheta(\psi)B + \frac{F}{m\Omega}(p' + en\Phi'),$$

$$q_\parallel = q_\vartheta(\psi)B + \frac{5F}{2m\Omega}pT',$$

where $u_\vartheta(\psi)$ and $q_\vartheta(\psi)$ are undetermined constants of integration.

The total first order flows for any species can be written as

$$n\vec{u} = nu_\vartheta \vec{B} + \frac{B}{m\Omega}(p' + en\Phi')R\hat{\phi}, \tag{3.15}$$

$$\vec{q} = q_\vartheta \vec{B} + \frac{5B}{2m\Omega}pT'R\hat{\phi}, \tag{3.16}$$

from which we can see that the constants of integration give the poloidal flows

$$\vec{u}_p = u_\vartheta(\psi)\vec{B}_p, \tag{3.17}$$

$$\vec{q}_p = q_\vartheta(\psi)\vec{B}_p. \tag{3.18}$$

3.2.6 Parallel Moment Balance

In equilibrium the parallel components of the fluid Eqs. 3.10 and 3.11 can be flux surface averaged to obtain

$$\left\langle \vec{B}\cdot\nabla\cdot\pi \right\rangle = \left\langle \vec{B}\cdot(\vec{F} + en\vec{E}) \right\rangle, \tag{3.19}$$

$$\left\langle \vec{B}\cdot\nabla\cdot\mathbf{R} \right\rangle - (3e/2m)p\left\langle \vec{B}\cdot\vec{E} \right\rangle - (e/m)\left\langle \vec{B}\cdot\vec{E}\cdot\mathbf{P} \right\rangle = \left\langle \vec{B}\cdot\vec{G} \right\rangle,$$

where $\pi = \mathbf{P} - p\mathbf{I}$ is the viscosity tensor. We can define two new quantities, the heat flux friction force

$$\vec{H} = (m/T)\vec{G} - (5/2)\vec{F} = -\int m\vec{v}(\frac{5}{2} - x^2)C(f)d\vec{v}$$

and the heat viscosity tensor

$$\Theta = (m/T)\mathbf{R} - (5/2)\mathbf{P} = -\int d^3v m(\frac{5}{2} - x^2)\vec{v}\vec{v}f$$

where $x^2 = v^2/v_T^2$. The heat viscosity tensor is traceless to lowest order in δ and can equivalently be expressed as

$$\Theta = -\int d^3v m(\frac{5}{2} - x_a^2)[\vec{v}\vec{v} - (v^2/3)\mathbf{I}]f$$

The second moment balance equation can then be rewritten as

$$\left\langle \vec{B}\cdot\nabla\cdot\Theta \right\rangle = \left\langle \vec{B}\cdot\vec{H} \right\rangle, \tag{3.20}$$

where we have neglected terms of $O(\delta^2)$ and have used

$$\left\langle \vec{B}\cdot\vec{E}\cdot\mathbf{P} \right\rangle = -p\left\langle \vec{B}\cdot\vec{E} \right\rangle + O(\delta^2).$$

3.2.7 The Friction-Flow Relations

The particle distribution function can be expanded in powers of δ

$$f_a = f_{a0} + f_{a1} + \cdots$$

where $f_{a0} = f_M$, the Maxwellian distribution function. When evaluating the friction forces, only the $\ell = 1$ spherical harmonic of the first order distribution function will contribute, since the collision operator is spherically symmetric in

velocity space. This $\ell = 1$ harmonic, denoted by $f_{a1}^{(1)}$, can be further expanded in terms of generalized Laguerre polynomials, $L_j^{(3/2)}(x_a^2)$, of order 3/2

$$f_{a1}^{(1)} = \frac{2\vec{v}}{v_T^2} \cdot \left[\sum_{j=0}^{\infty} \vec{u}_{aj} L_j^{(3/2)}(x_a^2)\right] f_{a0} \tag{3.21}$$

$$= \frac{2\vec{v}}{v_T^2} \cdot \left[\vec{u}_a - \frac{2}{5}\left(\frac{5}{2} - x_a^2\right)\frac{\vec{q}_a}{p_a} + \ldots\right] f_{a0}. \tag{3.22}$$

Here $x_a \equiv v/v_T$ and

$$n_a \vec{u}_{aj} = 3\frac{2^{(2j+1)} j!(j+1)!}{(2j+3)!} \int d^3v \vec{v} L_j^{3/2}(x_a^2) f_{a1}^{(1)}.$$

The first two coefficients in the expansion are identified as

$$\vec{u}_{a0} = \vec{u}_a,$$

$$\vec{u}_{a1} = -\frac{2\vec{q}_a}{5p_a},$$

where the heat flux is approximated, as in Eq. 3.21 by

$$\vec{q}_a = -T_a \int L_1^{(3/2)} \vec{v} f_{a1} d\vec{v}.$$

Using the expansion of $f_{a1}^{(1)}$, in the collision operator, linearized about f_{a0}, the friction forces can be expressed [5] as

$$\vec{F}_a = \sum_b \left[\ell_{11}^{ab} \vec{u}_b - \frac{2}{5}\ell_{12}^{ab}\frac{\vec{q}_b}{p_b} + \ldots\right],$$

$$\vec{H}_a = \sum_b \left[\ell_{21}^{ab} \vec{u}_b - \frac{2}{5}\ell_{22}^{ab}\frac{\vec{q}_b}{p_b} + \ldots\right],$$

where the friction coefficients ℓ_{ij}^{ab} can be written as

$$\ell_{ij}^{ab} = \left[\sum_k \frac{n_a m_a}{\tau_{ak}} M_{ak}^{i-1,j-1}\right]\delta_{ab} + \frac{n_a m_a}{\tau_{ab}} N_{ab}^{i-1,j-1}.$$

The matrix elements, $M_{ab}^{i-1,j-1}$ and $N_{ab}^{i-1,j-1}$ are moments of the collision operator:

$$\frac{n_a}{\tau_{ab}} M_{ab}^{ij} \equiv \int d^3v v_\| L_i^{(3/2)} C_{ab}\left(\frac{2v_\|}{v_{Ta}^2} L_j^{(3/2)} f_{a0}, f_{b0}\right),$$

$$\frac{n_a}{\tau_{ab}} N_{ab}^{ij} \equiv \int d^3v v_\| L_i^{(3/2)} C_{ab}\left(f_{a0}, \frac{2v_\|}{v_{Tb}^2} L_j^{(3/2)} f_{b0}\right),$$

where τ_{ab} is the Braginskii Coulomb collision time[18]

$$\tau_{ab} = \frac{3}{16\sqrt{\pi}} \frac{m_a^2 v_{Ta}^3}{n_b e_a^2 e_b^2 \ln\Lambda}.$$

The symmetry of the matrix elements

$$M_{ab}^{ij} = M_{ab}^{ji},$$

$$T_b^2 v_{Tb} N_{ab}^{ij} = T_a^2 v_{Ta} N_{ab}^{ji}$$

is due to the self-adjoint property [19] of the Coulomb collision operator. These relations lead to the symmetry of the friction coefficients

$$\ell_{ab}^{ij} = \ell_{ab}^{ji}.$$

The matrix elements are evaluated in reference [5]. The parallel friction forces can then be written as [20]

$$\vec{F}_e \cdot \vec{B} = -\vec{F}_i \cdot \vec{B} = [\ell^e_{11}(\vec{u}_i - \vec{u}_e) + \ell^e_{12}\frac{2\vec{q}_e}{5p_e}] \cdot \vec{B}, \tag{3.23}$$

$$\vec{H}_e \cdot \vec{B} = -[\ell^e_{12}(\vec{u}_i - \vec{u}_e) + \ell^e_{22}\frac{2\vec{q}_e}{5p_e}] \cdot \vec{B}, \tag{3.24}$$

$$\vec{H}_i \cdot \vec{B} = -\ell^i_{22}(\frac{2\vec{q}_i}{5p_i}) \cdot \vec{B}, \tag{3.25}$$

where terms of relative order m_e/m_i have been eliminated. Higher order terms in the expansion for the friction forces are not considered here.

The friction coefficients are

$$\ell^e_{11} = \frac{n_e m_e}{\tau_{ei}},$$

$$\ell^e_{12} = \ell^e_{21} = \frac{3}{2}\frac{n_e m_e}{\tau_{ei}},$$

$$\ell^e_{22} = (\frac{13}{4} + \sqrt{2})\frac{n_e m_e}{\tau_{ei}},$$

$$\ell^i_{22} = \sqrt{2}\frac{n_i m_i}{\tau_{ii}}.$$

The friction coefficients are independent of the collisionality regime, unlike the viscosity coefficients soon to be calculated.

3.2.8 Viscosity Coefficients

The dependence of the viscous forces on the first order flows $\vec{u}_a$ and $\vec{q}_a$ can now be deduced[21] for a neoclassical plasma. It can be assumed that, to lowest

order in the Larmor radius, the viscosity and heat viscosity tensors are linearly dependent on the spatial gradients of the first order flows. From Eqs. 3.15 and 3.16 it is clear that there are no first order flows across flux surfaces. Therefore there are no first order parallel viscous forces due to nonuniformities of the flow fields in the $\nabla\psi$ direction. Hence, the viscous forces must arise from gradients of the flows that lie within a magnetic flux surface. It is then clear that rigid body rotations of the plasma about the symmetry axis will give rise to no parallel viscous stress, even though adjacent flux surfaces may have different magnitudes of the toroidal flow. Thus the last terms in Eqs. 3.15 and 3.16 do not contribute to $\left\langle \vec{B} \cdot \nabla \cdot \pi \right\rangle$ or $\left\langle \vec{B} \cdot \nabla \cdot \Theta \right\rangle$. So the parallel viscous forces depend on the poloidal flows and have the form

$$\left\langle \vec{B} \cdot \nabla \cdot \pi_a \right\rangle = 3\left\langle (\hat{\eta} \cdot \nabla B)^2 \right\rangle \sum_b \left(\left(\mu^{ab}_{11} u_{\vartheta b} + \mu^{ab}_{12}\frac{2q_{\vartheta b}}{5p_b} \right), \right. \tag{3.26}$$

$$\left\langle \vec{B} \cdot \nabla \cdot \Theta_a \right\rangle = 3\left\langle (\hat{n} \cdot \nabla B)^2 \right\rangle \sum_b \left(\mu^{ab}_{21} u_{\vartheta b} + \mu^{ab}_{22}\frac{2q_{\vartheta b}}{5p_b} \right), \tag{3.27}$$

where the μ^{ab}_{ij} are collisionality dependent viscosity coefficients, and the overall factor of $3\left\langle (\hat{n} \cdot \nabla B)^2 \right\rangle$ is chosen so that μ^{aa}_{11} reduces to the classical value in the collisional limit. The inter-species coupling terms are small, since they arise from field-particle terms in the linearized collision operator [5], and will be dropped.

The standard technique used to calculate the viscosity coefficients is to find solutions in three asymptotic collisionality regimes and smooth these together to obtain a general solution. These three regimes are: (1) the collisionless (banana) regime, where trapped particle effects are dominant and trapped particles complete many drift orbits before undergoing a detrapping collision. (2) The intermediate (plateau) regime, where collision and bounce frequencies are comparable. (3) The collisional (fluid) regime where collisions dominate over trapped particle effects.

The Drift Kinetic Equation

These section, detailing the expansion of the DKE in powers of δ, closely follows the corresponding presentation by M.C. Zarnsrtorff[12]. The viscosity coefficients for the three collisionality regimes may be found using the kinetic Eq. 3.7. If this equation is averaged over the gyroangle [22], and terms of $O(\delta^2)$ are neglected we can obtain a steady state DKE for each species (a).

$$(\vec{v}_{\|} + \vec{v}_{Da}) \cdot \nabla \bar{f}_A + \frac{e_a}{m_a} \vec{v}_{\|} \cdot \partial_t \vec{A} \frac{\partial \bar{f}_a}{\partial \epsilon} = \sum_b C_{ab}(\bar{f}_a, \bar{f}_b).$$

The distribution function in this equation has been gyrophase averaged, $\vec{v}_{Da}$ is the perpendicular drift velocity, $\vec{A}$ is the vector potential, and $\epsilon = {}^1/_2 m_a v^2 + e_a \Phi(\psi)$ is the total particle energy. The overline notation will be dropped for

convenience.

If the distribution function is expanded in powers of δ, we find that the $O(\delta^0)$ solution is a Maxwellian. The $O(\delta)$ equation is

$$\vec{v}_{\|} \cdot \nabla f_{a1} + \vec{v}_{Da} \cdot \nabla \psi f'_{a0} - v_{\|} \frac{e_a E_{\|}}{T_a} f_{a0} = C_a(f_{a1}, f_{b1}) \tag{3.28}$$

where

$$C_a(f_{a1}, f_{b1}) = \sum_b [C_{ab}(f_{a1}, f_{b0}) + C_{ab}(f_{a0}, f_{b1})]$$

is the collision operator linearized about a Maxwellian. The first term of the linearized collision operator is the test particle term and the second is the field particle term.

The drift velocity is given by [23]

$$\vec{v}_{Da} = -v_{\|} \hat{n} \times \nabla \left(\frac{v_{\|}}{\Omega} \right)$$

which combined with the geometric relation

$$\hat{n} \times \nabla \psi = -F(\psi) \hat{n} + BR\hat{\phi},$$

and invoking axisymmetry, leads to

$$\begin{aligned} \vec{v}_{Da} \cdot \nabla \psi &= -F(\psi) v_{\|} (\hat{n} \cdot \nabla) \left(\frac{v_{\|}}{\Omega} \right) \\ &= F(\psi) \frac{(\hat{n} \cdot \nabla B)}{e_a B^2} \frac{m_a}{2} (v_{\|}^2 + v^2). \end{aligned}$$

Expand f_{a1} in terms of Legendre polynomials

$$f_{a1} = f_{a0} \sum_l A_{al}(\psi, \chi, v) P_l(\frac{v_\parallel}{v}),$$

where $P_0 = 1$, $P_1(x) = x$, and $P_2(x) = {}^1\!/_2(3x^2 - 1)$. Using the identities

$$(\hat{n} \cdot \nabla|_{E,\mu}) v_\parallel^2 = -v_\perp^2 \frac{(\hat{n} \cdot \nabla B)}{B}$$

and [24]

$$xP_l(x) = \frac{l+1}{2l+1} P_{l+1}(x) + \frac{l}{2l+1} P_{l-1}(x),$$

$$(1-x^2)\frac{\partial P_l(x)}{\partial x} = \frac{l(l+1)}{2l+1}[P_{l+1}(x) - P_{l+1}(x)],$$

in Eq. 3.28 will generate an infinite series of coupled differential equations

$$\begin{aligned} C_a^{(l)}(A_{al}, A_{bl}) \;=\; & v\frac{l}{2l-1}\left[\frac{(l-1)}{2}\frac{\hat{n}\cdot\nabla B}{B} + \hat{n}\cdot\nabla\right] f_{a0} A_{a(l-1)} \\ & + v\frac{l+1}{2l+3}\left[-\frac{(l+2)}{2}\frac{\hat{n}\cdot\nabla B}{B} + \hat{n}\cdot\nabla\right] f_{a0} A_{a(l+1)} \\ & - v\frac{e_a E_\parallel}{T_a}\delta_{l1} f_{a0} + F\frac{\hat{n}\cdot\nabla B}{e_a B^2} T_a x_a^2 \left(\frac{4}{3}\delta_{l0} + \frac{2}{3}\delta_{l2}\right) f_{a0}, \end{aligned} \tag{3.29}$$

where

$$C_a^{(l)}(A_{al}, A_{bl}) \equiv C_a(A_{al} P_l f_{a0}, A_{bl} P_l f_{b0})$$

We can further expand the v dependence of A_{al} in terms of Laguerre polynomials of order $l + {}^1\!/_2$,

$$A_{al} = x_a^l \sum_j a_{alj}(\psi, \chi) L_j^{(l+1/2)}(x_a^2),$$

where $x_a = v/v_{Ta}$, and

$$a_{alj}(\psi, \chi) = \frac{\int x_a^l L_j^{l+1/2}(x_a^2) P_l(v_\parallel/v) f_{a1} d\vec{v}}{\int x_a^{2l}[L_j^{l+1/2}(x_a^2) P_l(v_\parallel/v)]^2 f_{a0} d\vec{v}}.$$

The coefficients a_{alj} can in some cases be related to macroscopic plasma parameters such as

$$\begin{aligned} a_{a10} &= \frac{2}{v_{Ta}} u_{\parallel a}, \\ a_{a11} &= -\frac{2}{v_{Ta}}\frac{2q_{\parallel a}}{5p_a}, \\ a_{a20} &= \frac{2}{3}\frac{p_{\parallel a} - p_{\perp a}}{p_a}, \\ a_{a21} &= -\frac{4}{21}\frac{(\Theta_{\parallel a} - \Theta_{\perp a} + p_{\parallel a} - p_{\perp a})}{p_a}, \end{aligned} \tag{3.30}$$

where

$$p_{\parallel a} = \int m_a v_\parallel^2 f_{a1} d\vec{v},$$

$$p_{\perp a} = \int {}^1\!/_2 m_a v_\perp^2 f_{a1} d\vec{v},$$

$$\Theta_{\parallel a} = -\int m_a v_\parallel^2 L_1^{(3/2)} f_{a1} d\vec{v},$$

$$\Theta_{\perp a} = -\int {}^1\!/_2 m_a v_\perp^2 L_1^{(3/2)} f_{a1} d\vec{v}.$$

To first order in the gyroradius expansion the viscosity and heat viscosity tensors have the CGL form[25]

$$\pi_a = (p_{\|a} - p_{\perp a})(\hat{n}\hat{n} - \mathbf{I}/3) \tag{3.31}$$

$$\Theta_a = (\Theta_{\|a} - \Theta_{\perp a})(\hat{n}\hat{n} - \mathbf{I}/3) \tag{3.32}$$

At this point we introduce approximations which will lead to the calculation of the viscosity coefficients in the various collisionality regimes.

Collisional Regime

Using Eq. 3.29 for $l = 2$ we can neglect $l = 3$ moments of f_{a1}, since they are of order $\tau_{aa}/\tau_{aB} \ll 1$ (τ_{aB} is the thermal bounce time) relative to higher order terms. Then using the expansions for A_{a1} and A_{a2} (truncated after two terms), and Eqs. 3.15 and 3.16, we obtain

$$2x_a^2\left[u_{\vartheta a}L_0^{(3/2)} - \frac{2q_{\vartheta a}}{5p_a}L_1^{(3/2)}\right](\hat{n}\cdot\nabla B)P_2 f_{a0} = \sum_b C_{ab}(x_a^2(a_{a20} + a_{a21})P_2 f_{a0}, f_{b0})$$

where the field particle terms in the collision operator have been neglected Taking the $x^2 L_0^{(5/2)}P_2$ and $x^2 L_1^{(5/2)}P_2$ moments we get the coupled equations

$$\frac{3}{2}n_a\left(u_{\vartheta a} - \frac{2q_{\vartheta a}}{5p_a}\right) = \sum_{j=0}^{1} a_{a2j}\sum_b \int x_a^4 L_0^{(5/2)}P_2 C_{ab}(x_a^2 L_j^{(5/2)}P_2 f_{a0}, f_{b0})d^3v,$$

$$\frac{21}{4}n_a\frac{2q_{\vartheta a}}{5p_a} = \sum_{j=0}^{1} a_{a2j}\sum_b \int x_a^4 L_1^{(5/2)}P_2 C_{ab}(x_a^2 L_j^{(5/2)}P_2 f_{a0}, f_{b0})d^3v.$$

The matrix elements are found and equations inverted in reference [5]. The coefficients a_{a2j} are related to the viscous forces through Eqs. 3.31, 3.32, 3.26, and 3.27. Then for a hydrogen plasma the viscosity coefficients are

$$\mu_{11}^{ee} = \frac{n_e m_e}{\tau_{ee}}\lambda_{ee}^2\frac{0.731}{2}, \tag{3.33}$$

$$\mu_{12}^{ee} = \mu_{21}^{ee} = \frac{n_e m_e}{\tau_{ee}}\lambda_{ee}^2\frac{1.446}{2},$$

$$\mu_{22}^{ee} = \frac{n_e m_e}{\tau_{ee}}\lambda_{ee}^2\frac{6.675}{2},$$

$$\mu_{11}^{ii} = \frac{n_i m_i}{\tau_{ii}}\lambda_{ii}^2\frac{1.358}{2},$$

$$\mu_{12}^{ii} = \mu_{21}^{ii} = \frac{n_i m_i}{\tau_{ii}}\lambda_{ii}^2\frac{2.191}{2},$$

$$\mu_{22}^{ii} = \frac{n_i m_i}{\tau_{ii}}\lambda_{ii}^2\frac{6.921}{2},$$

where $\lambda_{aa} = v_{Ta}\tau_{aa}$ is the mean free path, and terms of order $(m_e/m_i)^{1/2}$ have been omitted.

Plateau Regime

Various methods[26][27] have been used to calculate viscosity coefficients in the intermediate regime. These calculations all assume $\delta_B \ll 1$ where

$$\delta_B = \frac{B_{max} - B_{min}}{B_{max} + B_{min}},$$

and B_{max} and B_{min} are the magnetic field strength maximum and minimum for a given flux surface. It will be shown in chapter 4 that this condition on the magnetic field modulation is not satisfied. Therefore the plateau regime calculations will not be applied to the Octupole.

In this regime the following conditions are satisfied:

$$\nu_{*a} \equiv \frac{L_c}{v_{Ta}\tau_a}\delta_B^{-3/2} > 1,$$

and

$$\frac{v_{Ta}\tau_a}{L_c} > 1,$$

where

$$L_c^2 = \left\langle B^2 \right\rangle / \left\langle (\hat{n}\cdot\nabla B)^2 \right\rangle$$

is the square of the connection length.

Starting with the first order DKE (Eq. 3.28), and an appropriate model[28] for the linearized collision operator $C_a(f_{a1})$, we can put the solution for f_{a1} in the form[29]

$$f_{a1} = P_1(\frac{v_\parallel}{v})\left[S_a(\psi,v)\frac{B}{< B^2 >^{1/2}}f_{a0} + F\frac{v}{\Omega_a}f'_{a0}\right] + h_{a1} \qquad (3.34)$$

where h_{a1} is the portion of the solution *localized* in velocity space[30]. Since the term h_{a1} is of order $(\tau_{aB}/\tau_a) \ll 1$ with respect to the first term[28], we can

determine S_a to this order by expanding it in terms of Laguerre polynomials giving

$$S_a(\psi,v) = \frac{2x_a}{v_{Ta}}\left[u_{\vartheta a} - \frac{2}{5}\frac{q_{\vartheta a}}{p_a}\right] < B^2 >^{1/2},$$

where the expansion has been truncated after two terms. Using this form for S_a, and substituting Eq. 3.34 into Eq. 3.28 we obtain an equation for h_{a1} in terms of $u_{\vartheta a}$ and $q_{\vartheta a}$.

At this point f_{a1} is known for the plateau regime and the CGL form of the viscosity tensors (Eqs. 3.31 and 3.32) can be evaluated and used in the parallel moment balance equations (3.19, 3.20) to obtain the viscosity coefficients for the plateau regime, valid for an arbitrary flux surface geometry[29]:

$$\mu_{11}^{aa} = \frac{n_a m_a}{\tau_{aa}}\lambda_{aa}L_c\frac{\sqrt{\pi}}{6}\Gamma(3), \qquad (3.35)$$

$$\mu_{12}^{aa} = \frac{n_a m_a}{\tau_{aa}}\lambda_{aa}L_c\frac{\sqrt{\pi}}{6}\left[\Gamma(4) - \frac{5}{2}\Gamma(3)\right],$$

$$\mu_{22}^{aa} = \frac{n_a m_a}{\tau_{aa}}\lambda_{aa}L_c\frac{\sqrt{\pi}}{6}\left[\Gamma(5) - 5\Gamma(4) - \frac{25}{4}\Gamma(3)\right].$$

Banana Regime

This regime exists for values of the collisionality parameter $\nu_{*a} < 1$. It is convenient to expand the distribution function and drift kinetic equation in powers of ν_{*a}. Using Eq. 3.28, the lowest order (ν_{*a}^0) equation,

$$v_{\|}\hat{n}\cdot\nabla\left(f_{a1}^{(0)}-F(\psi)f'_{a0}\frac{v_{\|}}{\Omega_a}\right)=0,$$

where $f_{a1}=f_{a1}^{(0)}+f_{a1}^{(1)}+\cdots$, can be solved to obtain

$$f_{a1}^{(0)}=F(\psi)\frac{v_{\|}}{\Omega_a}f'_{a0}+g_a(v,v_{\|},\psi), \tag{3.36}$$

where g_a is a constant of integration.

The next order ($\nu_a^{(1)}$) equation,

$$v_{\|}\hat{n}\cdot\nabla f_{a1}^{(1)}-v_{\|}\frac{e_aE_{\|}}{T_a}f_{a0}=C_a(f_{a1}^{(0)},f_{b1}^{(0)}), \tag{3.37}$$

can be used to find constraints on g_a, by integrating over a bounce orbit for both the trapped and circulating particles. For circulating particles we use the annihilation operator $\left\langle B/v_{\|}\right\rangle$ on Eq. 3.37 to obtain

$$-\frac{e_a}{T_a}\left\langle\vec{B}\cdot\vec{E}\right\rangle f_{a0}=\left\langle\frac{B}{v_{\|}}C_a(f_{a1}^{(0)},f_{b1}^{(0)})\right\rangle, \tag{3.38}$$

which has a solution of the form[31]

$$g_a=\frac{2V_{\|}(\lambda,v)G_a(\psi,v^2)}{v_{Ta}^2}f_{a0}$$

where $\lambda=\mu/E$ is the pitch angle, and

$$V_{\|}(\lambda,v)=\frac{\sigma v}{2}\left\langle B^2\right\rangle^{1/2}\int_{\lambda}^{\lambda_c}\frac{d\lambda'}{\left\langle(1-\lambda' B)^{1/2}\right\rangle},$$

where $\sigma=v_{\|}/|v_{\|}|$. For circulating particle the pitch angle is in the range $0\le\lambda\le\lambda_c$ where $\lambda_c=B_{max}^{-1}$. Note that for a uniform magnetic field $V_{\|}\to v_{\|}$.

For trapped particles we can integrate Eq. 3.37 over a closed *banana* orbit to obtain

$$\int\frac{dl_{\|}}{v_{\|}}C_a(g_a,g_b)=0$$

which implies $g_a=0$. For circulating particles we use the form for g_a in Eq. 3.36 and taking the $v_{\|}L_j^{3/2}$ moments for $j=0,1$ yields

$$g_a=\frac{2V_{\|}}{v_{Ta}^2}\frac{\left\langle B^2\right\rangle^{1/2}}{f_c}\left[u_{\vartheta a}(\psi)-\frac{2}{5}\frac{q_{\vartheta a}(\psi)}{p_a}L_1^{(3/2)}(x_a^2)\right]$$

where

$$f_c=\frac{3}{4}\left\langle B^2\right\rangle\int_0^{B_{max}^{-1}}\frac{\lambda\,d\lambda}{\left\langle(1-\lambda B)^{1/2}\right\rangle}$$

is the fraction of circulating particles. In reference [5] the expression for g_a is substituted into Eq. 3.37 and using Eq. 3.38 they obtain

$$v_{\|}\hat{n}\cdot\nabla f_{a1}^{(1)}=C_a(g_a,f_{b1}^{(0)})-\frac{V_{\|}H(\lambda_c-\lambda)}{f_c}\frac{\left\langle B^2\right\rangle^{1/2}}{B^2}\left\langle\frac{B}{v_{\|}}C_a(g_a,f_{b1}^{(0)})\right\rangle$$

where $H(\lambda_c-\lambda)$ is the Heaviside step function. Taking $v_{\|}L_j^{3/2}$ moments of this equation gives relations between $u_{\vartheta a}$, $q_{\vartheta a}$, and the viscous forces which can be solved to obtain viscosity coefficients for the banana regime as follows:

$$\mu_{11}^{ee} = \frac{n_e m_e}{\tau_{ee}} L_c^2 \frac{f_t}{f_c} \frac{1}{3} [\sqrt{2} - \ln(1+\sqrt{2}) + 1] \tag{3.39}$$

$$\mu_{12}^{ee} = \frac{n_e m_e}{\tau_{ee}} L_c^2 \frac{f_t}{f_c} \frac{1}{3} [-\frac{4}{\sqrt{2}} + \frac{5}{2}\ln(1+\sqrt{2}) - \frac{3}{2}]$$

$$\mu_{22}^{ee} = \frac{n_e m_e}{\tau_{ee}} L_c^2 \frac{f_t}{f_c} \frac{1}{3} [\frac{39}{4\sqrt{2}} - \frac{25}{4}\ln(1+\sqrt{2}) + \frac{13}{4}]$$

$$\mu_{11}^{ii} = \frac{n_i m_i}{\tau_{ii}} L_c^2 \frac{f_t}{f_c} \frac{1}{3} [\sqrt{2} - \ln(1+\sqrt{2})]$$

$$\mu_{12}^{ii} = \frac{n_i m_i}{\tau_{ii}} L_c^2 \frac{f_t}{f_c} \frac{1}{3} [-\frac{4}{\sqrt{2}} + \frac{5}{2}\ln(1+\sqrt{2})]$$

$$\mu_{22}^{ii} = \frac{n_i m_i}{\tau_{ii}} L_c^2 \frac{f_t}{f_c} \frac{1}{3} [\frac{39}{4\sqrt{2}} - \frac{25}{4}\ln(1+\sqrt{2})]$$

where $f_t = 1 - f_c$ is the fraction of trapped particles and terms of order $(m_e/m_i)^{1/2}$ have been dropped.

Smoothing the Viscosity Coefficients

At this point the viscosity coefficients derived above are only valid in the appropriate collisionality regime. It is necessary to derive smoothed coefficients valid for arbitrary collisionality. Since some of the coefficients change sign from one regime to another, it is convenient to define a positive definite coefficient matrix[5] given by

$$K_{11}^a = \mu_{11}^{aa}, \tag{3.40}$$

$$K_{12}^a = K_{21}^a = \mu_{12}^{aa} + \frac{5}{2}\mu_{11}^{aa},$$

$$K_{22}^a = \mu_{22}^{aa} + 5\mu_{12}^{aa} + \frac{25}{4}\mu_{11}^{aa}.$$

Using this matrix reference [5] describes a smoothed form for the coefficients with

$$K_{ij}^a(\nu_{\tau a}) = \frac{K_{ij}^{aPS} K_{ij}^{aP} K_{ij}^{aB}}{[K_{ij}^{aPS} + K_{ij}^{aP}][K_{ij}^{aP} + K_{ij}^{aB}]} \tag{3.41}$$

where K_{ij}^{aPS}, K_{ij}^{aP}, and K_{ij}^{aB} are the coefficients evaluated in the Pfirsch-Schlüter, plateau, and banana regimes respectively. It is shown[5] that this smoothed form for the coefficients is good in the banana and Phirsch-Schlüter regimes but may give poor results in the plateau regime. With this caveat in mind, the above method of smoothing coefficients will be used, as opposed to more accurate formalisms that are tedious to apply.

3.2.9 Calculation of the Currents

Inserting the equations for particle and heat flux (3.15 and 3.16), and the friction-flow and viscosity-flow relations (Eqs. 3.23-3.27), into the parallel moment balance equations (3.19 and 3.20), we obtain a set of coupled equations that can be solved to find the flows $u_{\vartheta a}$ and $q_{\vartheta a}$ in terms of the friction and

viscosity coefficients:

$$3\left\langle(\hat{n}\cdot\nabla B)^2\right\rangle(\mu_{11}^{ee}u_{\vartheta e}+\mu_{12}^{ee}\frac{2q_{\vartheta e}}{5p_e})$$
$$= l_{11}^e\left[(u_{\vartheta i}-u_{\vartheta e})\left\langle B^2\right\rangle+\frac{F}{e}\left(\frac{p_i'}{n_i}+\frac{p_e'}{n_e}\right)\right]$$
$$+l_{12}^e\left[\frac{2q_{\vartheta e}}{5p_e}\left\langle B^2\right\rangle-\frac{F}{e}T_e'\right]-n_e e\left\langle\vec{\mathrm{B}}\cdot\vec{\mathrm{E}}\right\rangle,$$

$$3\left\langle(\hat{n}\cdot\nabla B)^2\right\rangle(\mu_{11}^{ii}u_{\vartheta e}+\mu_{12}^{ii}\frac{2q_{\vartheta e}}{5p_e})$$
$$= -l_{11}^e\left[(u_{\vartheta i}-u_{\vartheta e}\left\langle B^2\right\rangle+\frac{F}{e}\left(\frac{p_i'}{n_i}+\frac{p_e'}{n_e}\right)\right]$$
$$-l_{12}^e\left[\frac{2q_{\vartheta e}}{5p_e}\left\langle B^2\right\rangle-\frac{F}{e}T_e'\right]+n_i e\left\langle\vec{\mathrm{B}}\cdot\vec{\mathrm{E}}\right\rangle,$$

$$3\left\langle(\hat{n}\cdot\nabla B)^2\right\rangle(\mu_{21}^{ee}u_{\vartheta e}+\mu_{22}^{ee}\frac{2q_{\vartheta e}}{5p_e})$$
$$= -l_{21}^e\left[(u_{\vartheta i}-u_{\vartheta e}\left\langle B^2\right\rangle+\frac{F}{e}\left(\frac{p_i'}{n_i}+\frac{p_e'}{n_e}\right)\right]$$
$$-l_{22}^e\left[\frac{2q_{\vartheta e}}{5p_e}\left\langle B^2\right\rangle-\frac{F}{e}T_e'\right],$$

$$3\left\langle(\hat{n}\cdot\nabla B)^2\right\rangle(\mu_{21}^{ii}u_{\vartheta i}+\mu_{22}^{ii}\frac{2q_{\vartheta i}}{5p_i})=-l_{22}^i\left[\frac{2q_{\vartheta i}}{5p_i}\left\langle B^2\right\rangle+\frac{F}{e}T_i'\right]$$

Inverting these equations we can get a direct expression for the parallel current

$$j_{\|}=\frac{Fp'}{B}-\frac{FB_p}{\langle B^2\rangle}\left[\frac{p'}{p}(1-\hat{L}_{31})-\frac{T_e'}{T}\hat{L}_{32}-\frac{T_i'}{T}\hat{L}_{32}^i\right]+\sigma_{NC}\frac{\left\langle\vec{\mathrm{B}}\cdot\vec{\mathrm{E}}\right\rangle}{\langle B^2\rangle}\vec{\mathrm{B}}. \quad (3.42)$$

where $p=p_e+p_i$, $T=T_e+T_i$ and the $\hat{L}_{ij}$ are normalized transport coefficients. These transport coefficients are related to elements of the Onsager matrix and are given by

$$\hat{L}_{31}=\frac{\hat{\mu}_{11}^e(l_{22}^e+\hat{\mu}_{22}^e)+\hat{\mu}_{12}^e(l_{12}^e-\hat{\mu}_{12}^e)}{(\hat{\mu}_{11}^e+l_{11}^e)(l_{22}^e+\hat{\mu}_{22}^e)-(l_{12}^e-\hat{\mu}_{12}^e)^2}, \quad (3.43)$$

$$\hat{L}_{32}=\frac{\hat{\mu}_{12}^e(l_{22}^e+\hat{\mu}_{22}^e)+\hat{\mu}_{22}^e(l_{12}^e-\hat{\mu}_{12}^e)}{(\hat{\mu}_{11}^e+l_{11}^e)(l_{22}^e+\hat{\mu}_{22}^e)-(l_{12}^e-\hat{\mu}_{12}^e)^2},$$

$$\hat{L}_{32}^i=\hat{L}_{31}\frac{\hat{\mu}_{12}^i l_{22}^i}{\hat{\mu}_{11}^i(l_{22}^i+\hat{\mu}_{22}^i)-(\hat{\mu}_{12}^i)^2},$$

$$\sigma_{NC}=(ne)^2\frac{l_{22}^e+\hat{\mu}_{22}^e}{(\hat{\mu}_{11}^e+l_{11}^e)(l_{22}^e+\hat{\mu}_{22}^e)-(l_{12}^e-\hat{\mu}_{12}^e)^2},$$

where $\hat{\mu}_{ij}=\mu_{ij}\frac{3\left\langle(\hat{n}\cdot\nabla B)^2\right\rangle}{\langle B^2\rangle}$, and terms of order $(m_e/m_i)^{1/2}$ have been neglected.

3.3 Application to the Octupole

Calculated positions of the Octupole flux surfaces are generated by the program SOAK[32][33]. This program includes the time dependent perturbations of the flux surfaces due to the finite conductivity of the boundary conductors. From the results of this code the flux surfaces can be traced, to allow

the calculation of the flux surface averages needed to determine the parallel current.

The typical magnetic field modulation and circulating particle fraction, δ_B and f_c respectively, are shown in Figs. 3-3 and 3-4. The field modulation is large enough that the plateau regime approximations are inappropriate, especially in the common flux region where $\psi > 5.7$. We can see that the fraction of circulating particle is less than half the total, and that in the common flux region nearly all ($\geq$90%) of the particles are trapped. Since the plateau regime is absent, Eq. 3.41 is replaced with

$$K_{ij}^{a}(v_{Ta}) = \frac{K_{ij}^{aPS} K_{ij}^{aB}}{[K_{ij}^{aPS} + K_{ij}^{aB}]}, \tag{3.44}$$

for the purpose of smoothing the viscosity coefficients between the collisional and banana regimes. This approximation will be accurate enough for the purpose of comparing Octupole currents with theory.

Figs. 3-5 through 3-7 demonstrate the calculated dependence of the electron viscosity coefficients on λ_{ee}, for a flux surface inside the separatrix. These coefficients have a similar dependence on λ_{ee} in the common flux region. Using the smoothed viscosity coefficients, Fig. 3-8 shows the dependence of the coefficient $1 - \widehat{L}_{31}$ on λ_{ee}. As seen in Figs. 3-9 and 3-10 this coefficient has a weak dependence on $\vec{B}_t$ and ψ.

In Fig. 3-11 the relative magnitudes of the coefficients $1 - \widehat{L}_{31}$, $\widehat{L}_{32}$, and $\widehat{L}_{32}^{i}$ are shown. Since the typical plasma has $\frac{p'}{p} \gg \frac{T_e'}{T} \simeq \frac{T_i'}{T}$ (see sec. 4.1), we will find that the parallel current is predominately driven by pressure gradients. For comparison of non-ohmic Octupole plasmas with theory, only the terms in Eq. 3.42 that are proportional to the pressure gradient will be used.

The calculated dependence of the neoclassical conductivety σ_{NC} on the electron mean free path is shown in Fig. 3-12 in units of $ne^2\tau_{ee}/m_e$. On this scale the Spitzer conductivity has a value of 2. As the viscous stress between trapped and circulating particles increases, the magnitude of σ_{NC} rapidly decreases from the Spitzer value to its banana regime limit.

Fig. 3-1. Theory Flow Chart

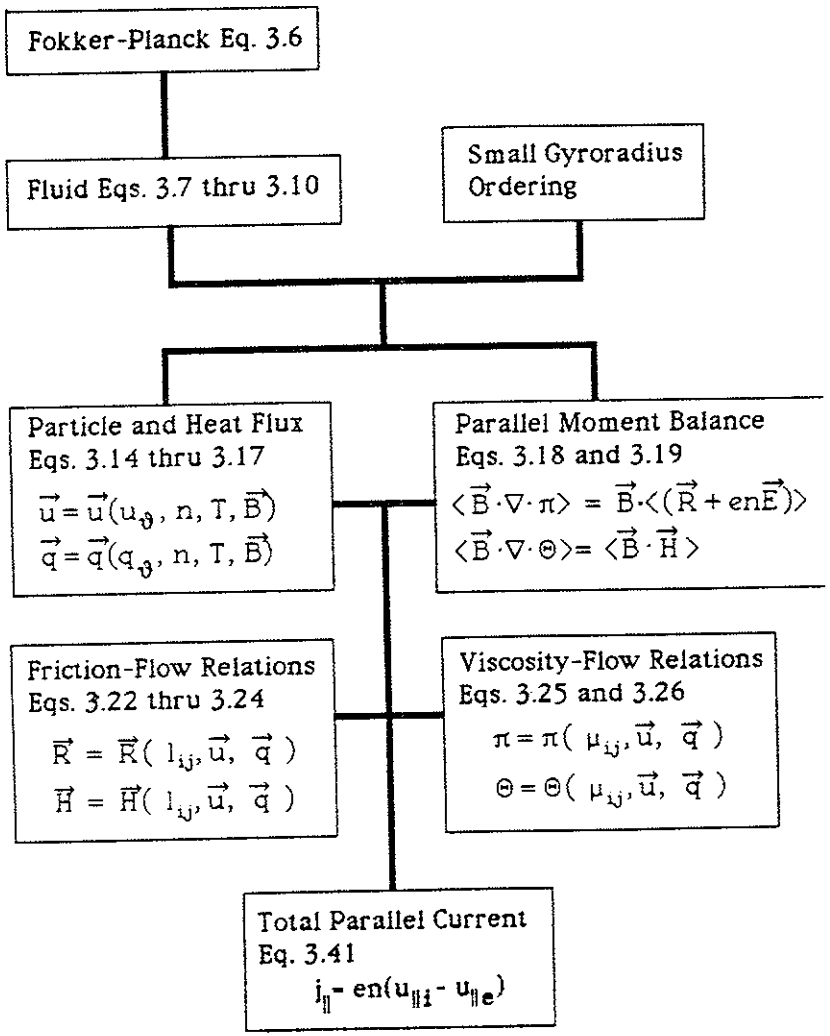

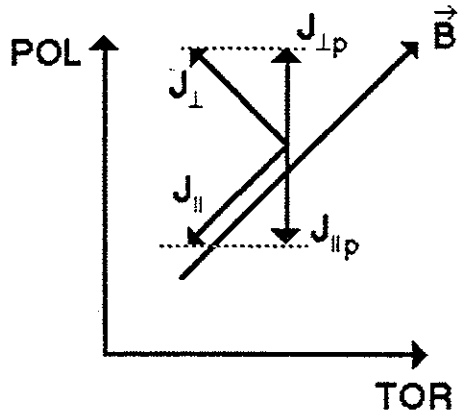

Fig. 3-2. Bootstrap current is generated by the viscous force between trapped and untrapped particles. When poloidal viscosity is high the plasma generates the parallel bootstrap current to insure the poloidal current is nearly zero.

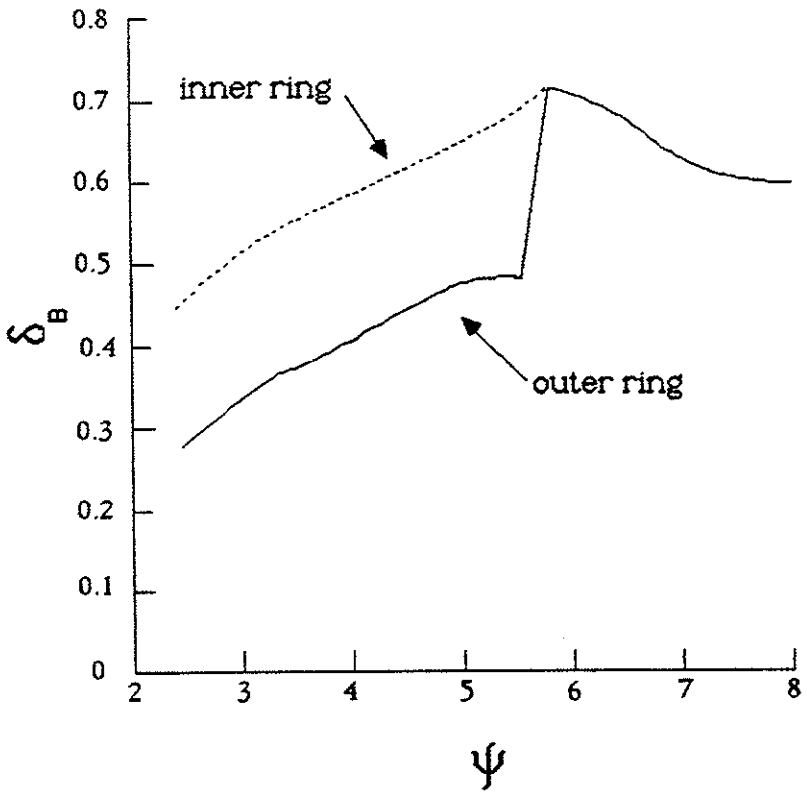

Fig. 3-3. The calculated flux-surface dependence of the magnetic field modulation, for B_t= 370 G on the separatrix.

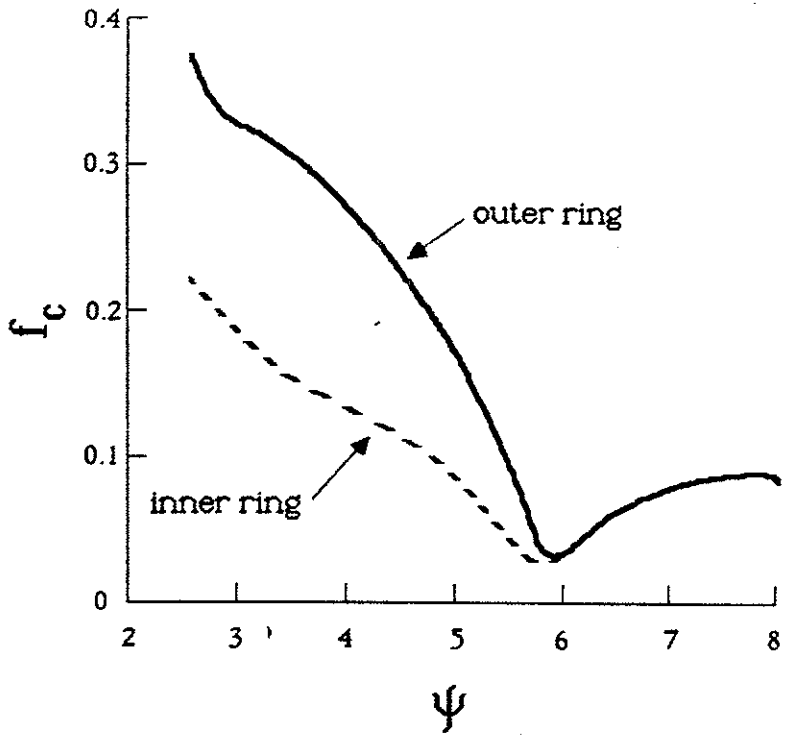

Fig. 3-4. The calculated flux-surface dependence of the circulating particle fraction for B_t= 370 G on the separatrix.

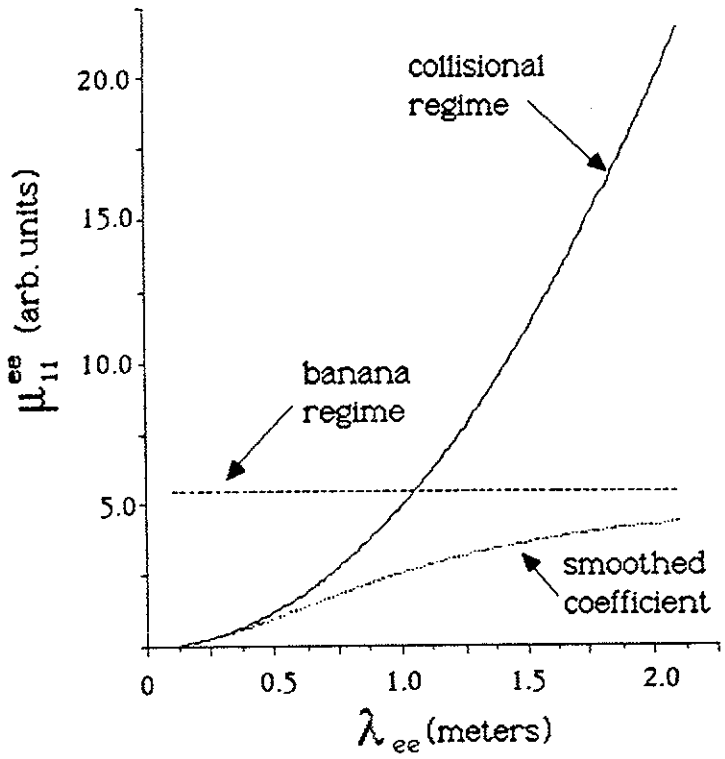

Fig. 3-5. This figure illustrates the dependence of μ_{11}^{ee} on λ_{ee} for the collisional regime, banana regime, and for the smoothed coefficient (Eqs. 3.33, 3.39, and 3.44 respectively). This is calculated for the flux surface $\psi = 4.5$ with $B_p = 1240$ G and $B_t = 380$ G.

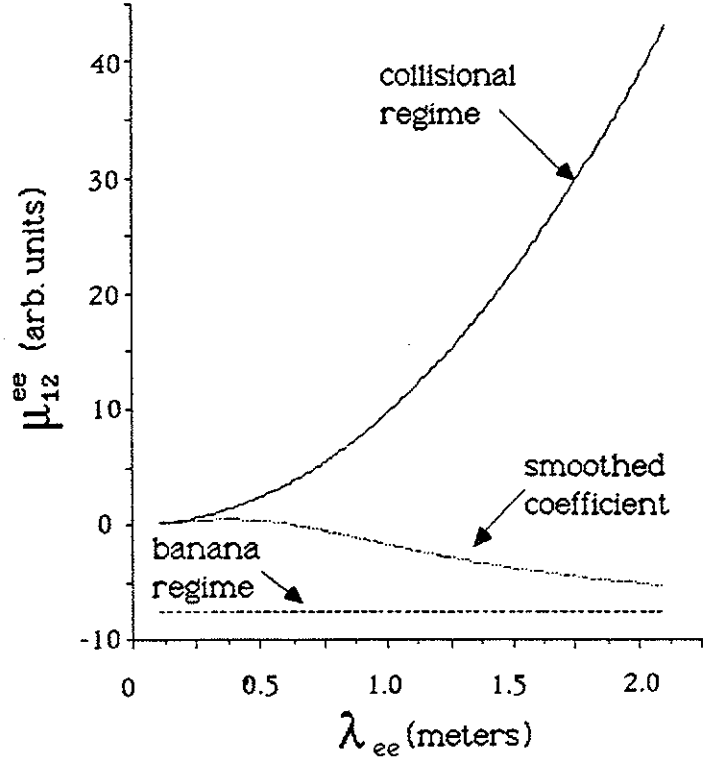

Fig. 3-6. This figure illustrates the dependence of μ_{12}^{ee} on λ_{ee} for the collisional regime, banana regime, and for the smoothed coefficient (Eqs. 3.33, 3.39, and 3.44 respectively). This is calculated for the flux surface $\psi = 4.5$ with $B_p = 1240$ G and $B_t = 380$ G.

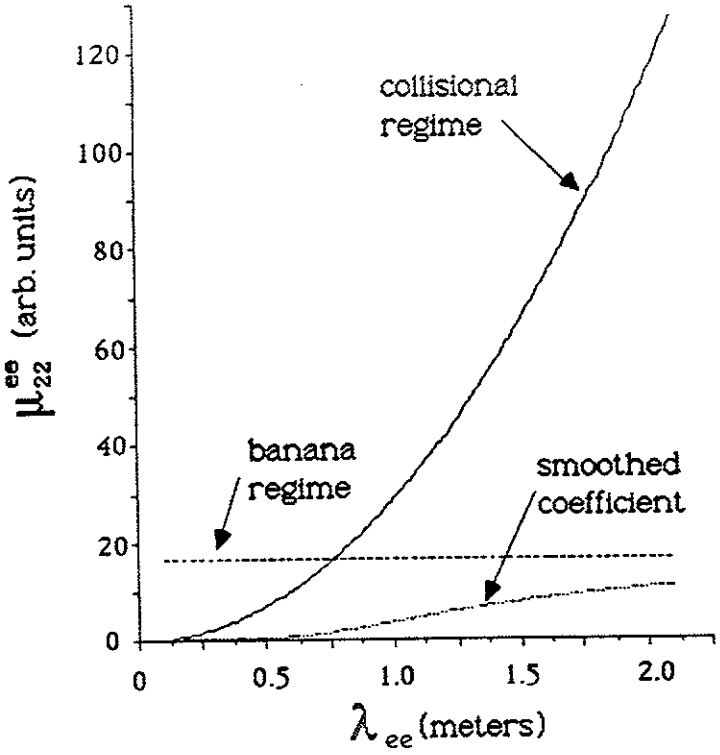

Fig. 3-7. This figure illustrates the dependence of μ_{22}^{ee} on λ_{ee} for the collisional regime, banana regime, and for the smoothed coefficient (Eqs. 3.33, 3.39, and 3.44 respectively). This is calculated for the flux surface $\psi = 4.5$ with $B_p = 1240$ G and $B_t = 380$ G.

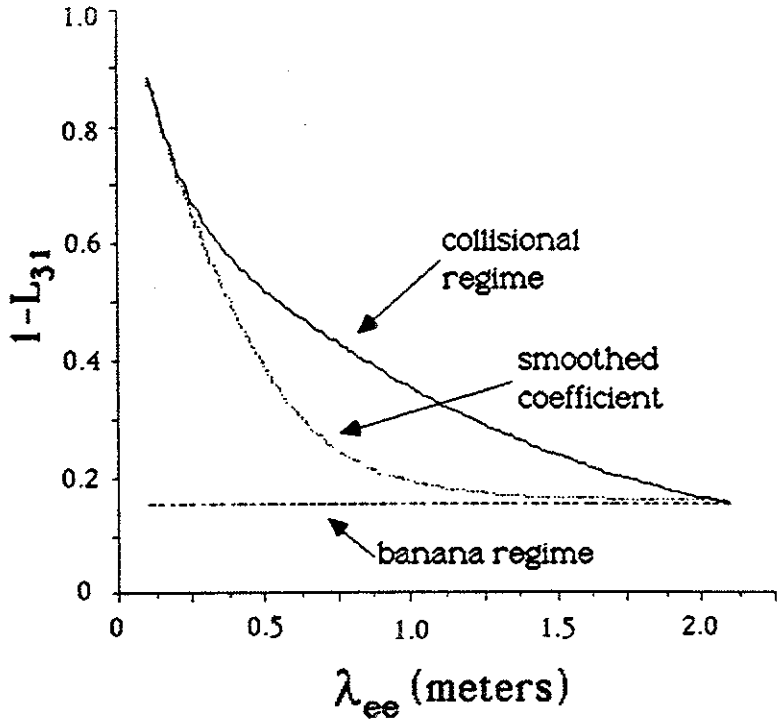

Fig. 3-8. Calculated dependence of $(1-L_{31})$ on λ_{ee} (Eq. 3.43), for $\psi = 4.5$, $B_p = 1240$ G, and $B_t = 380$ G on the separatrix.

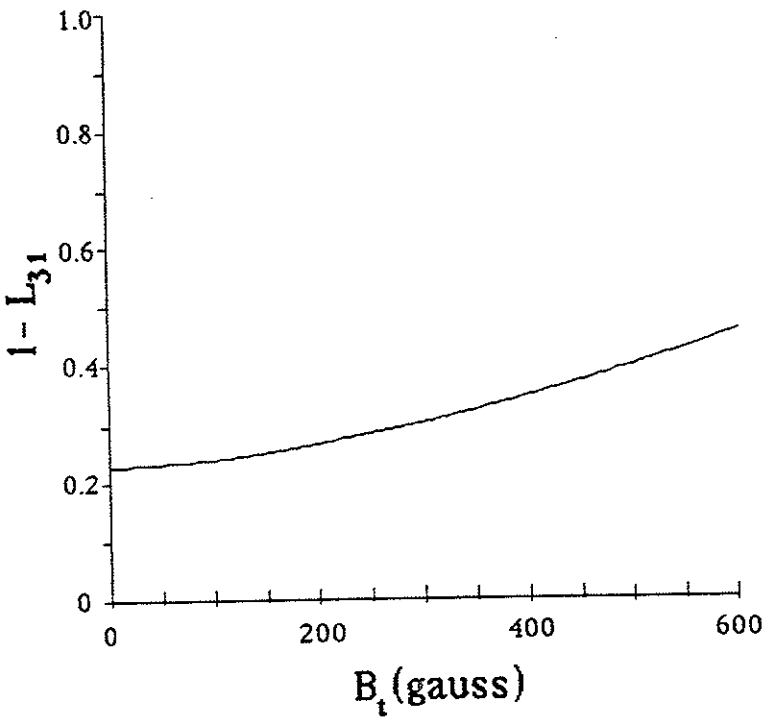

Fig. 3-9. Dependence of calculated value of $(1-L_{31})$ on B_t, for $\psi=4.5$ and $\lambda_{ee}= 1.0$ m.

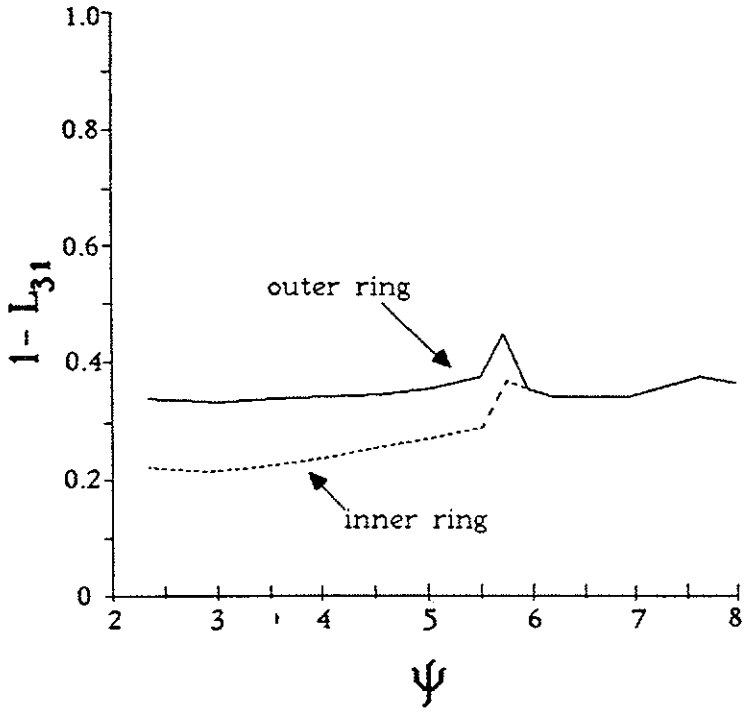

Fig. 3-10. Dependence of calculated value of $(1-L_{31})$ on ψ, for $B_t=370$ G on the separatrix and $\lambda_{ee}= 1.0$ m.

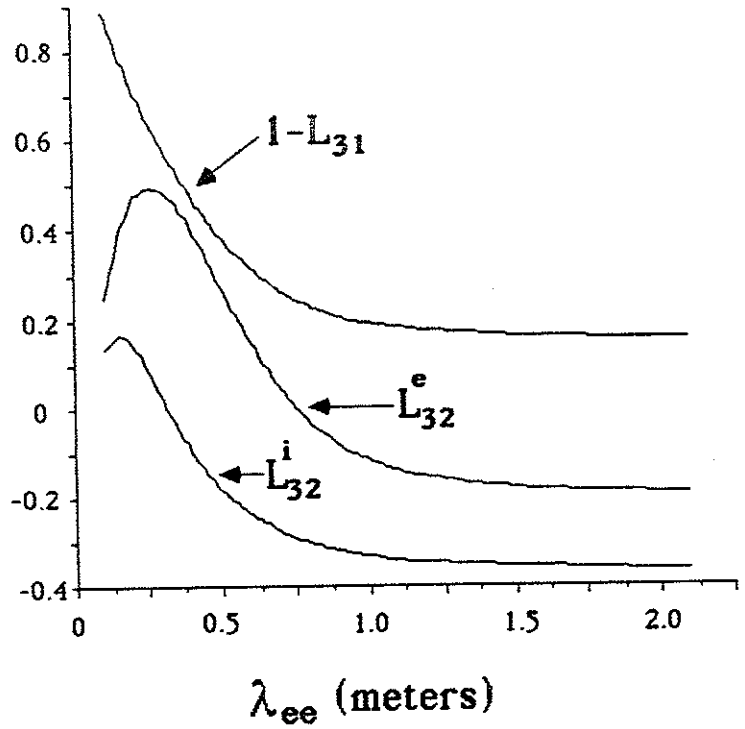

Fig. 3-11. The relative magnitude of the coefficients $(1-L_{31})$, L^{e}_{32}, and L^{i}_{32} are shown for $\psi=4.5$, with $B_p=1240$ G and $B_t=380$ G.

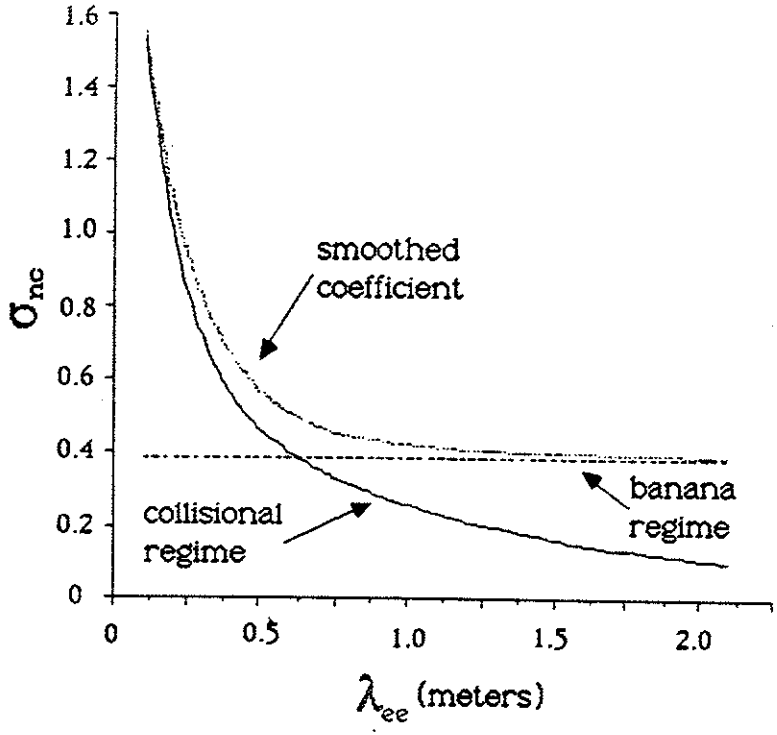

Fig. 3-12. Dependence of the neoclassical conductivety on the collisionality λ_{ee}, for $\psi=4.5$, $B_p=1240$ G, and $B_t=380$ G.

Chapter 4

Experimental Results

This chapter will discuss the experimental results germaine to this investigation. We will start with a description of the general plasma parameters for typical plasmas created in this experiment. These parameters will be valid for plasmas with and without ohmic currents, since the ohmic currents caused negligible plasma heating. The next topic will be current density measurements at the flux surfaces $\psi = 4.5$, 5.0, and 6.0, for plasmas with no ohmic current. The parallel current density and the pressure gradient associated with the diamagnetic current will be discussed and compared with theory. Next we will look at plasmas with ohmic currents on the flux surface $\psi = 4.5$ and see how the ohmic current scales with the toroidal electric field.

Also discussed in this chapter is the axisymmetry of the Octupole plasmas. When the data in this section was taken it was never intended that it would be used as part of this investigation. It was originally intended to be a short investigation into how field errors in the Octupole might be affecting local measurements of density and temperature. It was later realized that either the field errors or the anomalous local plasma parameters might be affecting the current density measurements and therefore this data was resurrected. It should be realized, when reading this section, that the data is incomplete in terms of relating field errors to measurements of current density.

The last topic discussed in this chapter will be the main differences between the results shown in this thesis and the results presented by M.C. Zarnstorff[12][13][14].

4.1 General Plasma Parameters

The measurement of typical plasma parameters and plasma currents was done in the lower outer bridge region (Fig. 4-1) of the Octupole at a toroidal angle of $45° - 55°$ from the primary core. In this region the radial distance from the ring to the wall is 11 cm and the separatrix is 5 cm from the ring. In Fig.

4-2 the density profile in the bridge (measured by langmuir probe) is shown to be approximately gaussian, and peaks on the separatrix early in time. As the profile evolves the density peak moves in towards the ring and the density in the private flux initially increases while the common flux density decreases. It has been speculated that the inward motion of the density profile is caused by enhanced tranport[17] in the common flux region. In Fig. 4-3 we see that the peak in pressure also moves in towards the ring with time, but unlike the density, the pressure decreases everywhere. From the temperature profile, in Fig. 4-4, we see that the electron temperature initially peaks near the internal ring, but by 1.5 msec after plasma injection the temperature profile is relatively flat. From the radial profile of λ_{ee} in Fig. 4-5 it is seen that initially the plasma is relatively collisionless ($\lambda_{ee} \geq 80$ cm, see Fig. 3-6) and that by 1.5 msec after plasma injection the plasma near the separatrix is collisional with $\lambda \leq 30\ cm < L_e$. In Fig. 4-6 a comparison is made between the magnitudes of the inverse pressure and temperature gradient scale lengths. We see that in general the temperature gradient terms in Eq. 3.38 will be negligible, and are subsequently ignored when comparing the measured parallel currents with theory.

In order to ascertain the reliability of magnetic probe measurements, we

can compare pressure gradients calculated from pressure profiles taken with a Langmuir probe, and pressure gradients calculated from diamagnetic current measurements made with the magnetic probes. In Fig. 4-7 we have a measurement of the pressure gradient at $\psi = 4.5$ that compares results from both a magnetic probe and a Langmuir probe. Figs. 4-11 and 4-14 make similar comparisons for the flux surfaces 5.0 and 6.0. On the flux surfaces 4.5 and 5.0 these two diagnostics are in agreement, which lends confidence to the results of the current density measurements discussed below and indicates that the diamagnetic currents in the Octupole are as expected from Eq. 3.2. It should be noted that $\psi = 6.0$ is near the separatrix, where from Fig. 4-3 we see that the pressure measurements have large error bars. Therefore, pressure gradient measurements made with the Langmuir probe at $\psi = 6.0$ are less reliable than measurements at the flux surfaces 4.5 and 5.0.

4.2 Current Density Measurements

4.2.1 Normal Plasmas (No Ohmic Currents)

The flux surface $\psi = 4.5$ is in the private flux region, about 2 cm in from the separatrix in the lower outer bridge. The parallel current at $\psi = 4.5$

(Fig. 4-8) is unusual in that the current magnitude, as measured by magnetic probe, initially increases at a time when the pressure gradient is decreasing (Fig. 4-7). The only other quantity that is increasing at this time is the density, as previously mentioned. Fig. 4-9 shows how the measured parallel current (normalized to the pressure gradient) varies with λ_{ee}, as the plasma decays during a single shot. The dashed line is the theoretical prediction from Eq. 3.42. We see that the parallel current has a sign opposite from the predictions and a magnitude that is too large.

The flux surface $\psi = 5.0$ is also in the private flux region, about 1.2 cm from the separatrix. At $\psi = 5.0$ the parallel current in Fig. 4-10 decreases monotonically with time, as expected from the pressure gradient time decay in Fig. 4-11. However, the magnitude of the parallel current is clearly larger at $\psi = 5.0$ than at $\psi = 4.5$ for times before 3 msec. This is contrary to what is expected from Eq. 3.42 since λ_{ee} is nearly the same on each surface (Fig. 4-5) and the pressure gradient at $\psi = 4.5$ is in general greater than that at $\psi = 5.0$. Specifically, if we look at time $t = 1.0$ msec, we have $j_{\|}|_{\psi=5.0} \simeq 2j_{\|}|_{\psi=4.5}$ and $p'|_{\psi=5.0} \simeq \frac{2}{5}p'|_{\psi=4.5}$. Fig. 4-12 demonstrates the same disparity between the measured and calculated $j_{\|}$ at $\psi = 5.0$ as was seen at $\psi = 4.5$.

The flux surface $\psi = 6.0$ is in the common flux region (0.4 cm from the

separatrix), where the pressure gradient reverses sign from its value in the private flux region. From Eq. 3.42 we would also expect the parallel current to reverse sign. In Fig. 4-13 we see that $j_{\|}$ is in the same direction as it is in the private flux and has about the same magnitude as $j_{\|}$ at $\psi = 5.0$. The pressure gradient in Fig 4-14 has indeed reversed sign from its value in the private flux region and has a magnitude about the same as the $\psi = 4.5$ pressure gradient. Comparing the measured ratio of $j_{\|}/p'$ to the theoretical curve in Fig. 4-15 we see that the parallel current has the correct sign in the banana regime but has a magnitude that is much too large. In the collisional regime the direction of the current is opposite from the expected Pfirsch-Schlüter current.

On all these flux surfaces the theory predicts that the parallel current will reverse sign as the plasma collisionality increases. For these plasmas this means that the parallel current must initially decay away faster than the pressure gradients driving it. Since the reverse case is true, there seems to be more parallel current being driven than can be accounted for by considering the perpendicular pressure gradients alone.

4.2.2 Plasma with Ohmic Currents

Plasmas were created with the addition of toroidal ohmic currents of the same order of magnitude as the usual parallel and perpendicular currents. Fig. 4-16 shows two cases where the ohmic currents were driven in opposite directions. In each case the magnitude of the driving electric field was the same. In order to determine if the ohmic currents had any effect on the usual parallel current these two cases were averaged and compared with a case where there was no ohmic current in Fig. 4-17. We see that when the effects of the ohmic currents are averaged out the result is the usual parallel current. This result is consistent with the idea that the ohmic current and the non-ohmic parallel current linearly superpose.

By separating the ohmic current from the non-ohmic parallel current, it is shown in Fig. 4-18 that the ohmic current depends linearly on the toroidal electric field, as is expected from Eq. 3.42. For $\lambda_{ee} = 20$ cm the local plasma conductivity should be about half the Spitzer value, which gives a predicted j_{ohmic} about three times the measured value. Previous measurements[34][35] of the flux surface averaged conductivity in the Octupole have found values consistent with the neoclassical theory in the collisional regime and at intermediate collisionality.

It should be pointed out that all these current measurements are local, and may be subject to the local effects of asymmetry discussed in the next section.

4.3 Axisymmetry of the Plasma

The assumption of an axisymmetric plasma, in the theory of neoclassical currents, gives us the flux surface constant $K(\psi) \propto j_p$. If this assumption is unwarranted, then the measured plasma currents will be dependent on the toroidal angle and the extent of the deviation from axisymmetry.

An investigation into the profile of the Octupole plasmas has shown that they are not axisymmetric. Magnetic field errors have been traced to fields leaking through the poloidal gap[37] due to an inappropriate distribution of the primary field windings on the iron core. The distribution of poloidal wall current, creating the toroidal field, was also found to be non-axisymmetric. The current driven in the vacuum vessel walls, in order to create the toroidal magnetic field, was found to create a small time dependent poloidal magnetic field also. This nonaxisymmetry of the toroidal field was probably caused by an uneven distribution of wall current, due to unmatched contact resistances of the electrical connections to the vacuum vessel.

Fig. 4-19 shows how the δB_p generated by the plasma currents at $\psi = 7.0$ varies as B_t is increased. The relationship seems random, except for a narrow range of toroidal field values where the signal peaks. Fig. 4-20 demonstrates how the gradient in the plasma generated δB_p varies during a scan of B_t. Again we see a random behavior with a sharp peak that coincides with the peak in δB_p. To lowest order $j_t \propto \nabla(\delta B_p)$ (Eq. 2.4) and will contain components both perpendicular and parallel to the magnetic field. A similar random scaling of $j_\parallel$ with B_t in the common flux region was seen by M.C. Zarnstorff[12].

One effect of the field error on the plasma was the existence of a flux tube with anomalously low plasma temperature. As the ratio of B_t to B_p is increased from zero, and the pitch of the field lines increase, this tube of flux can be placed at successive Langmuir probes, distributed in either the poloidal or toroidal direction. Fig. 4-21 demonstrates how the ion saturation current to one of these probes undergoes a large reduction in magnitude at the same toroidal field strength that the magnetic signals in Figs. 4-18 and 4-19 have their peak. At the ratio B_t/B_p where this flux tube is in the lower outer bridge at the toroidal angle $\phi = 45°$ the j_{sat} signal at $\phi = 55°$ seems normal. Fig. 4-22 shows a radial profile of the ratio of the saturation currents at $\phi = 45°$ and $\phi = 55°$ in the lower outer bridge. Throughout the profile

the probes were moved together, therefore if the plasma was axisymmetric the ratio of the signals should remain constant. We see that outside the separatrix there is as much as a 50% decrease in the magnitude of the signal at $\phi = 45°$. Inside the separatrix there are indications of an asymmetry of a lesser extent. This toroidal asymmetry in the ion saturation current indicates that there are probably pressure gradients along a flux surface, near the region of this flux tube with cooler plasma.

For different toroidal and poloidal probe positions the onset of this *dip* in the current to a Langmuir probe occurs at different values of B_t. These differences in the onset of the dip are consistent with results expected if cool plasma localized to a flux tube existed. This dip in the saturation current occurs primarily in the common flux region. This cooler flux tube of plasma was mapped back to the poloidal gap midplane, where it is supposed that field errors caused plasma scrap-off as field lines grazed the vacuum vessel, which in turn introduced cold particles from the wall.

Attempts were made to eliminate the errors in the poloidal field by re-arranging the distribution of the primary windings of the core. These attempts were only marginally successful. No attempts were made to correct the toroidal field errors since gaining access to the electrical connections at

the vacuum vessel was extremely difficult, and would have resulted in several weeks of work where the Octupole would be nonoperational.

4.4 Comparison to Past Octupole Experiments

When the disparity between the results of this thesis and the results presented by Zarnstorff were first discovered much work went into resolving the unfortunate conflict. Reaching a consensus was hampered by the fact that the discrepancy was discovered about one year after the shutdown of the Octupole program. The reasons for this disparity were finally pinpointed and are discussed below.

First there was a difference in data analysis techniques. Initially we used the same data analysis programs, but as our experiments evolved in different directions so did the data analysis methods. The experiments required two sets of integrators with different relative gains. The difference in gain (a factor of 4.7) could be taken into account during the process of the final data analyses or when archiving the data (i.e., recording the scale factor). Initially the first process was used, but at some point, unknown to me, Zarnstorff switched to the latter method. Application of my analysis programs to Zarnstorff's data

gave results similar to what I have presented in this thesis. The pertinent data records needed to insure proper analysis of Zarnstorff's data no longer existed.

The other major difference was in the measurement of $\delta\nabla B$ when the magnetic probe was aligned with the toroidal direction, thus effectively measuring the poloidal current. Zarnstorff's signals were about half of what I measured for the flux surface $\psi = 4.5$. It is this flux surface where Zarnstoff found that the collisionality dependence of the parallel current was neoclassical. The difference in the measured $\delta\nabla B$ is consistent in data I've taken during a period of over a year, and not easily accounted for as a one-time mistake. This signal is not *raw* data since the difference between the signals of the two coils in the probe is calculated and then integrated before it is recorded. The individual coil signals are not recorded.

The nature of either of these differences was to cause a discrepancy in the calculation of the poloidal current (the toroidal current was essentially the same in each experiment) which lead to a difference in the parallel current with little difference in the diamagnetic current.

Although these differences have been pinpointed, the question of who made a mistake, if anyone did at all, has *not* been resolved, therefore the reader

should consider these results with this caveat in mind.

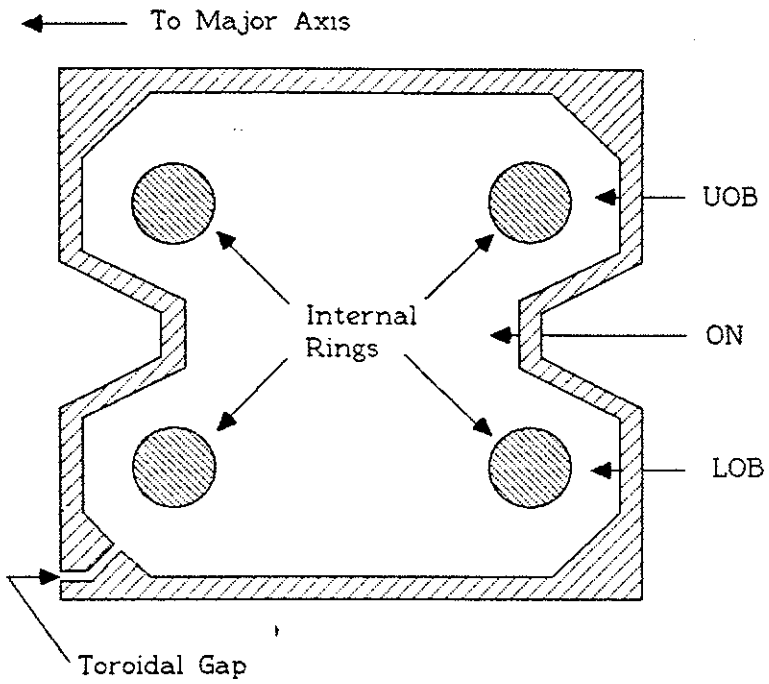

Fig. 4-1. Poloidal cross section of the Wisconsin Levitated Octupole.

Key: UOB – upper outer bridge
ON – outer nose
LOB – lower outer bridge

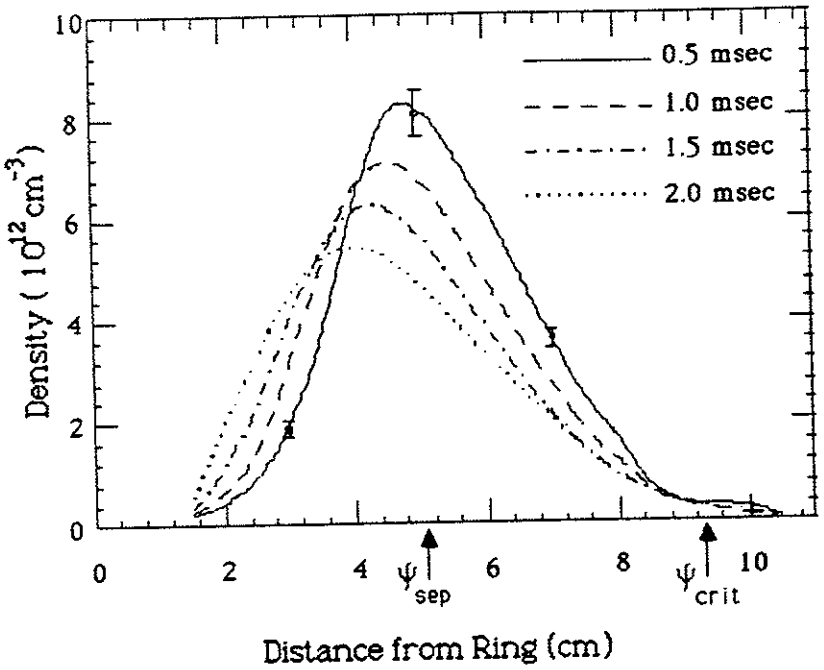

Fig. 4-2. Profile of the electron density in the lower outer bridge for $B_t = 370$ G on the separatrix.

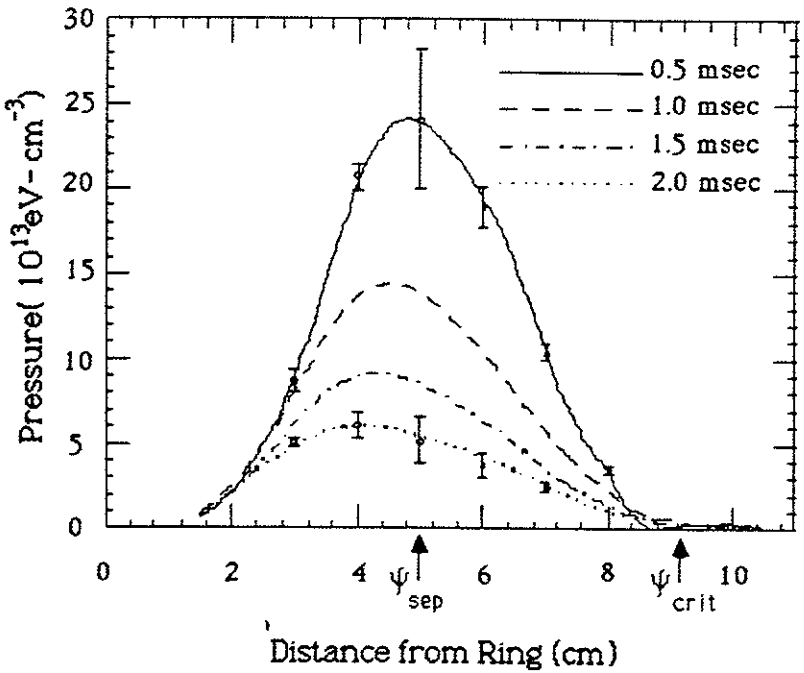

Fig. 4-3. Profile of the total plasma pressure in the lower outer bridge for $B_t = 370$ G on the separatrix.

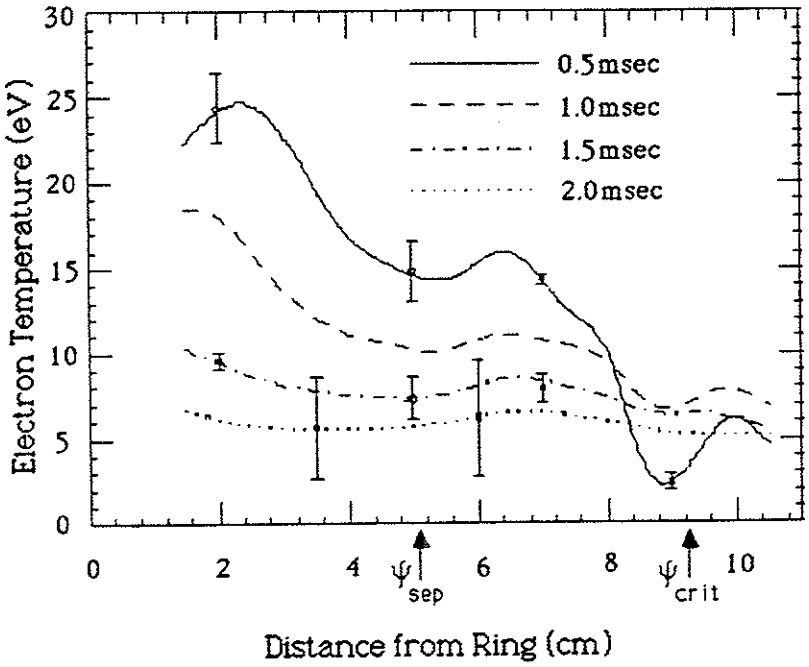

Fig. 4-4. Profile of the electron temperature in the lower outer bridge for $B_t = 370$ G on the separatrix.

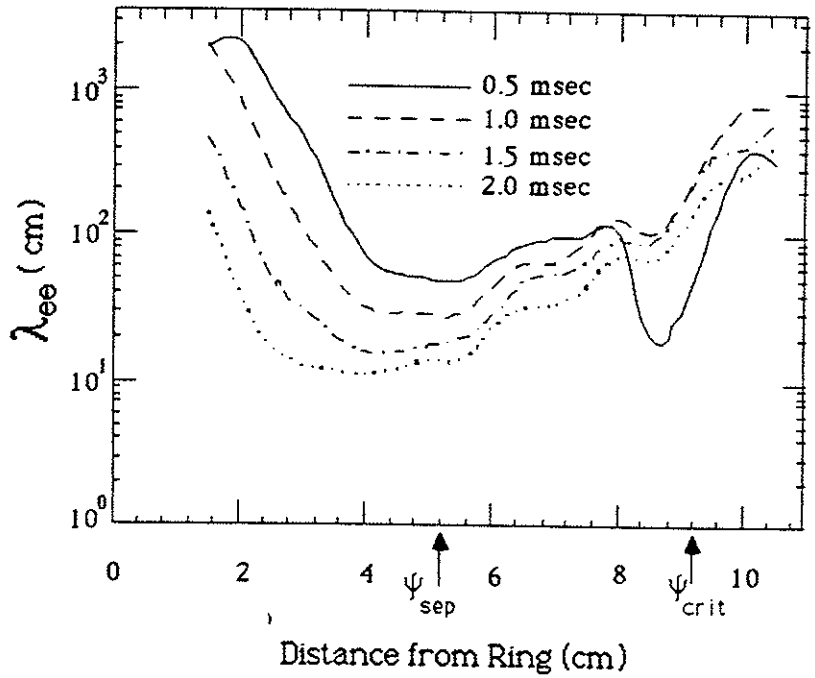

Fig. 4-5. Profile of the electron mean free path in the lower outer bridge for $B_t = 370$ G on the separatrix.

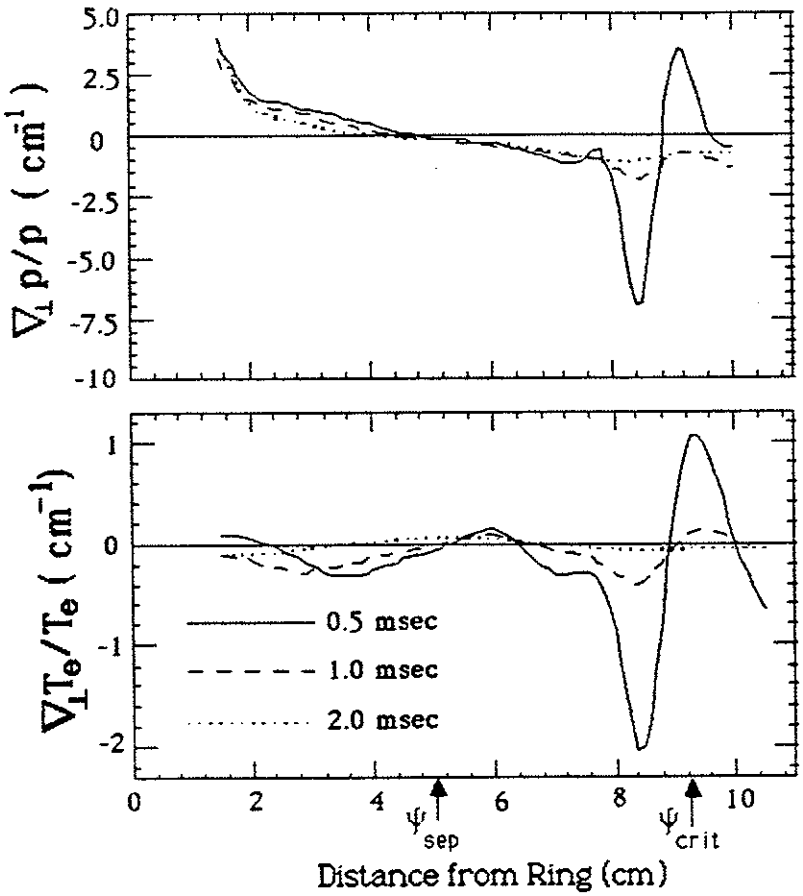

Fig. 4-6. Lower outer bridge profiles of the inverse gradient scale lengths that drive the parallel currents. $B_t = 370$ G on the separatrix.

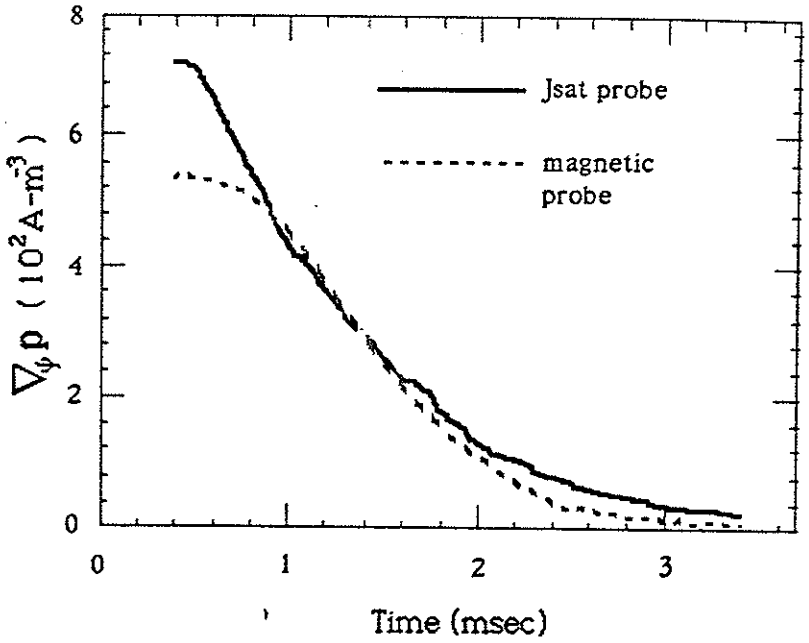

Fig. 4-7. Time decay of the pressure gradient measured with a magnetic probe and an ion saturation current probe. $\psi = 4.5$, $B_p = 1240$ G, and $B_t = 380$ G.

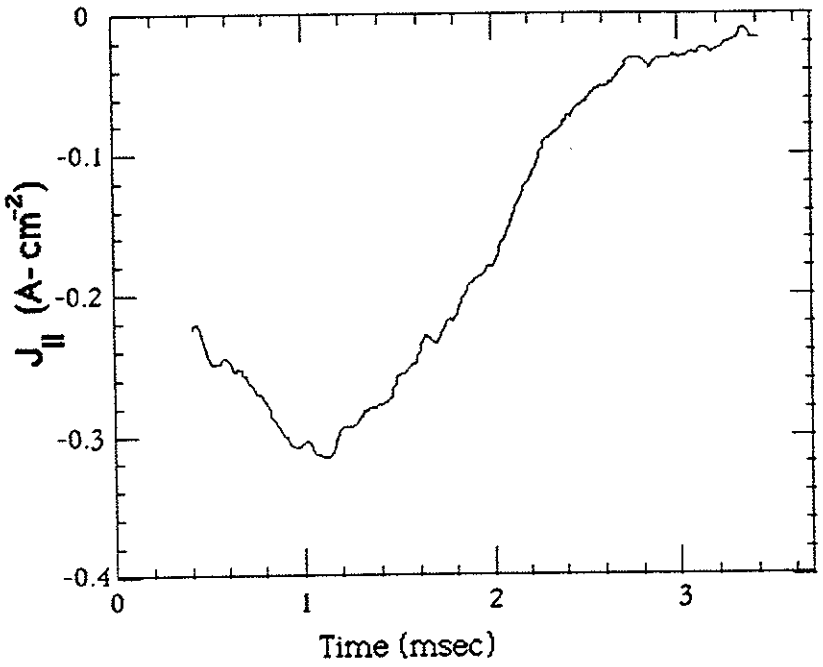

Fig. 4-8. Time dependence of the parallel current at $\psi = 4.5$, for $B_p = 1240$ G and $B_t = 380$ G.

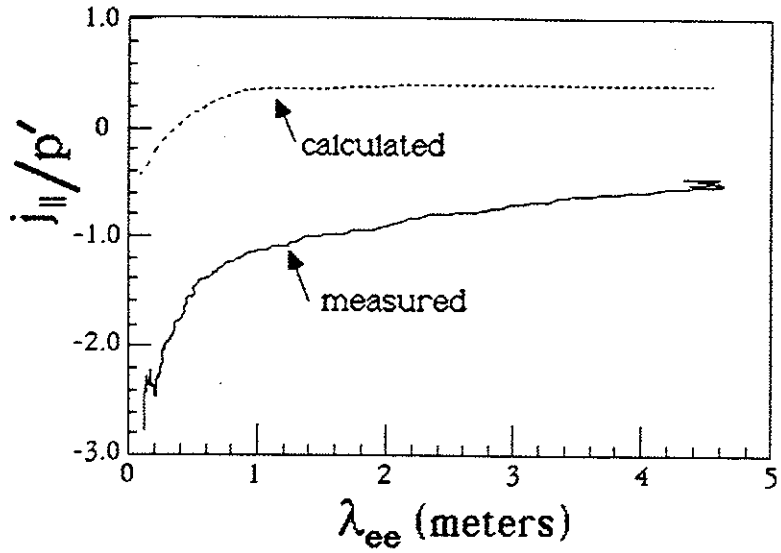

Fig. 4-9. Collisionality dependence of the ratio of the parallel current to the pressure gradient at $\psi = 4.5$, for $B_p = 1240$ G and $B_t = 380$ G.

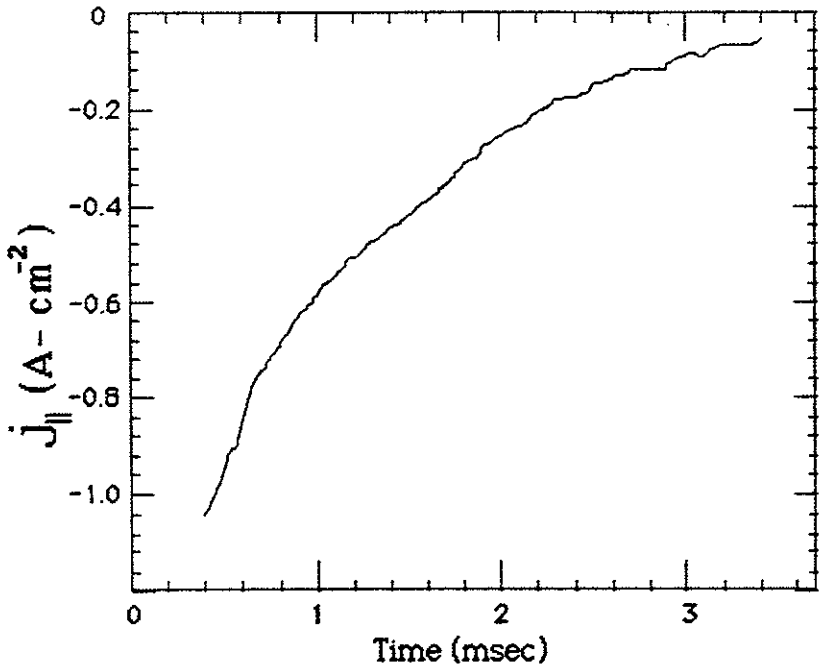

Fig. 4-10. Time dependence of the parallel current at $\psi = 5.0$, for $B_p = 1170$ G and $B_t = 380$ G.

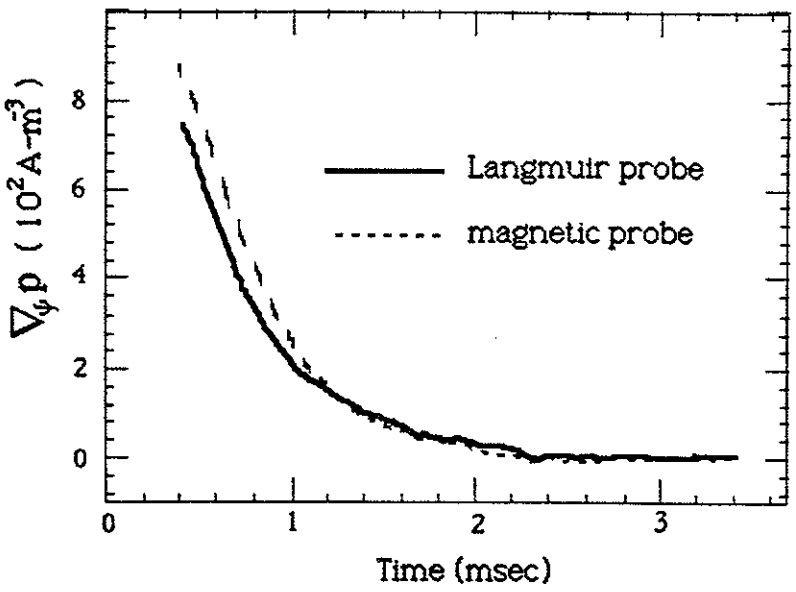

Fig. 4-11. Time decay of the pressure gradient measured at $\psi = 5.0$, for $B_p = 1240$ G, and $B_t = 380$ G with both a magnetic probe and a Langmuir probe.

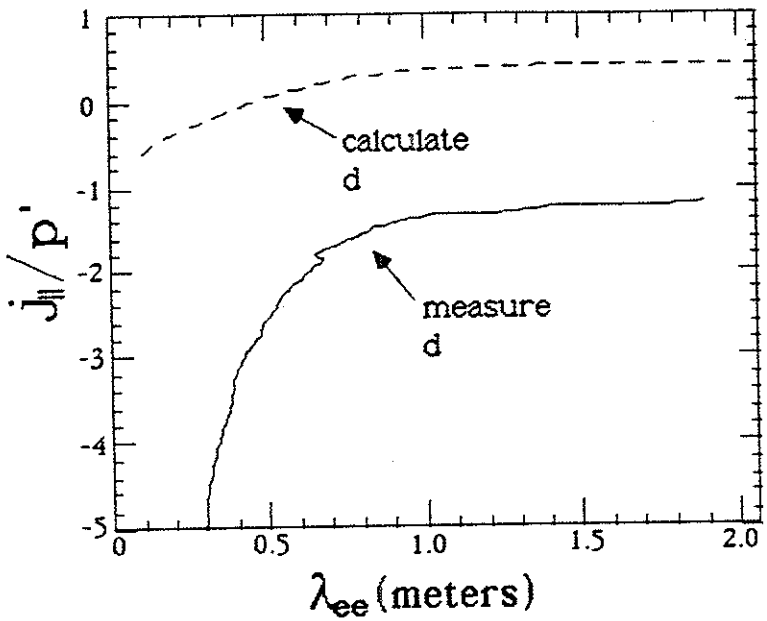

Fig. 4-12. Collisionality dependence of the ratio of the parallel current and the pressure gradient at $\psi=5.0$, for $B_p=1170$ G and $B_t=380$ G.

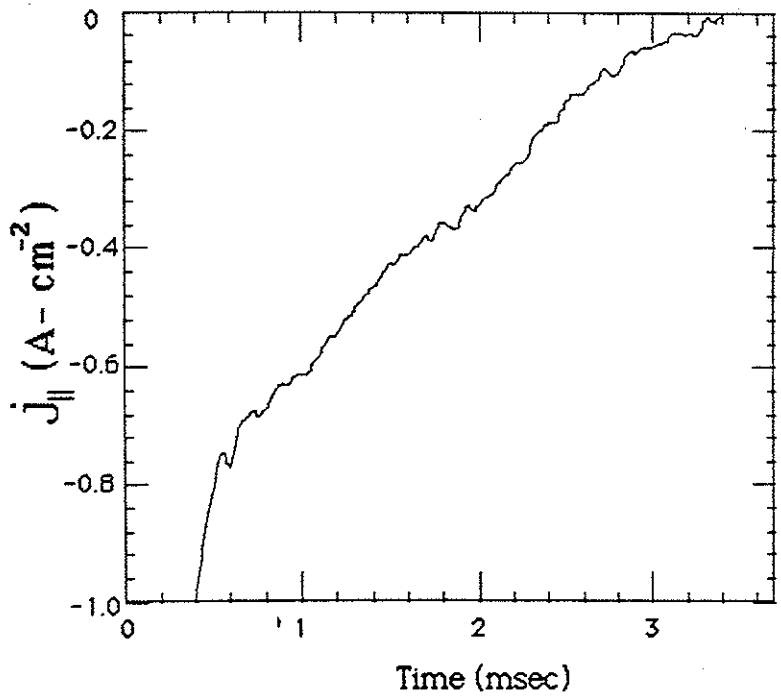

Fig. 4-13. Time dependence of the parallel current at $\psi=6.0$, for $B_p=970$ G and $B_t=360$ G.

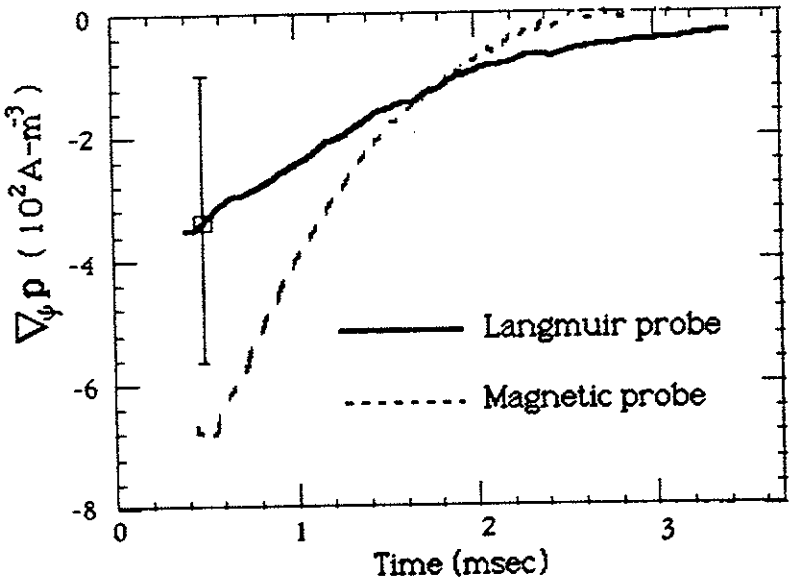

Fig. 4-14. Time decay of the pressure gradient measured at $\psi = 6.0$, for $B_p = 970$ G, and $B_t = 360$ G with both a magnetic probe and a Langmuir probe.

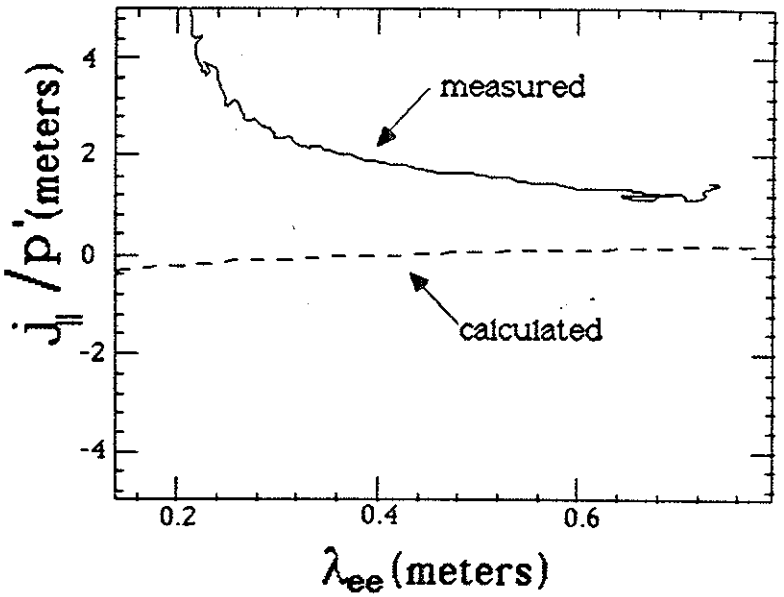

Fig. 4-15. Collisionality dependence of the ratio of the parallel current and the pressure gradient at $\psi = 6.0$, for $B_p = 960$ G and $B_t = 360$ G.

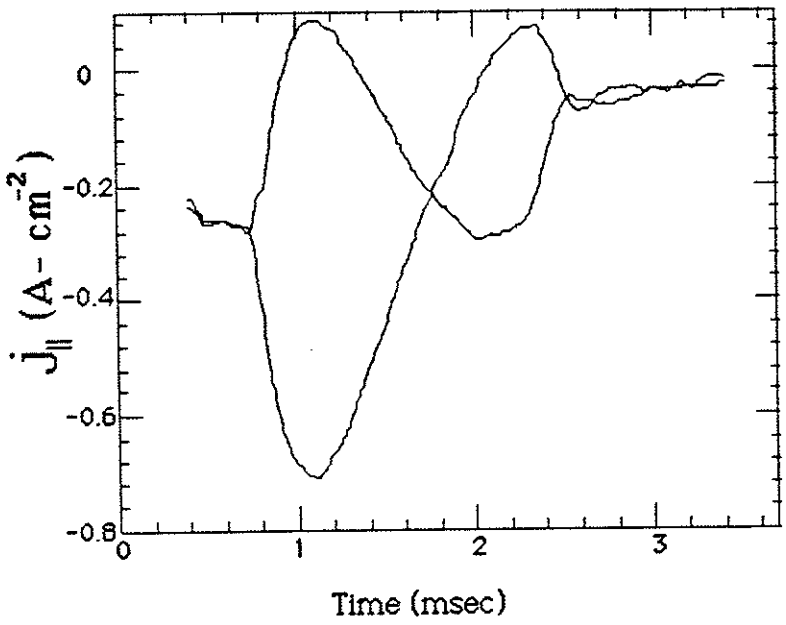

Fig. 4-16. Time dependence of the parallel current with the addition of ohmic current directed in both the positive and negative toroidal directions. $\psi = 5.0$, for $B_p = 1170$ G and $B_t = 380$ G.

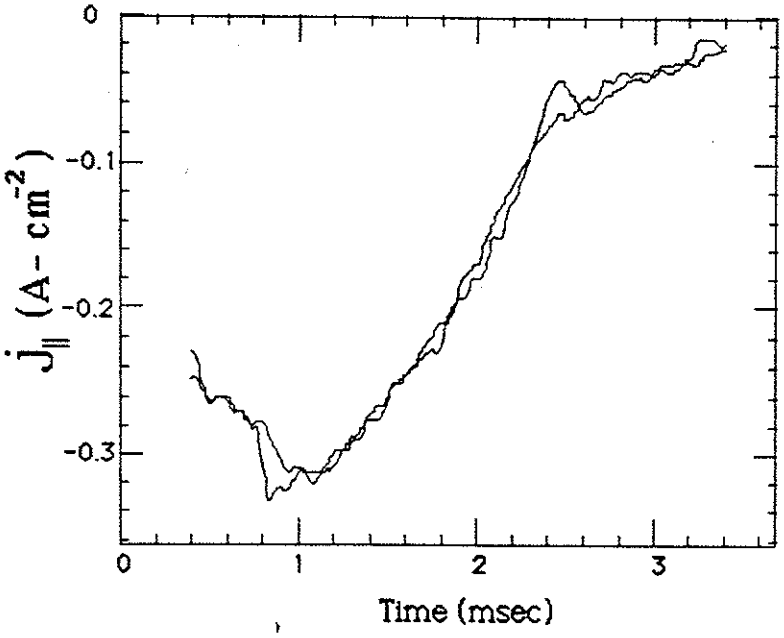

Fig. 4-17. Time dependence of the parallel current where one curve is a plasma without ohmic current and the other curve is the average of the two curves in Fig. 4-16. $\psi = 5.0$, for $B_p = 1170$ G and $B_t = 380$ G.

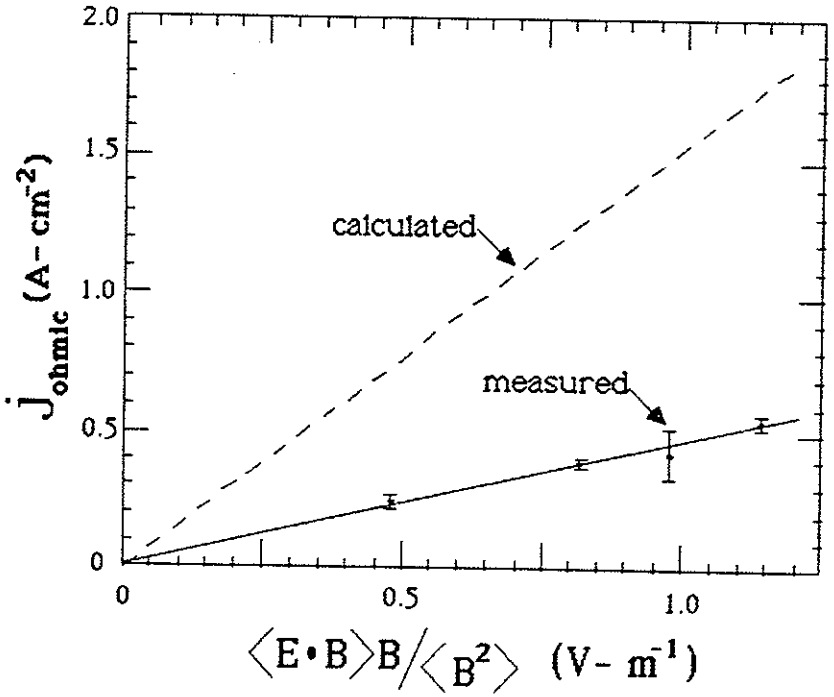

Fig. 4-18. The measured ohmic current is compared to the theoretically expected value at $\psi = 4.5$, for $\lambda_{ee} = 20$cm, $B_p = 1240$ G and $B_t = 380$ G.

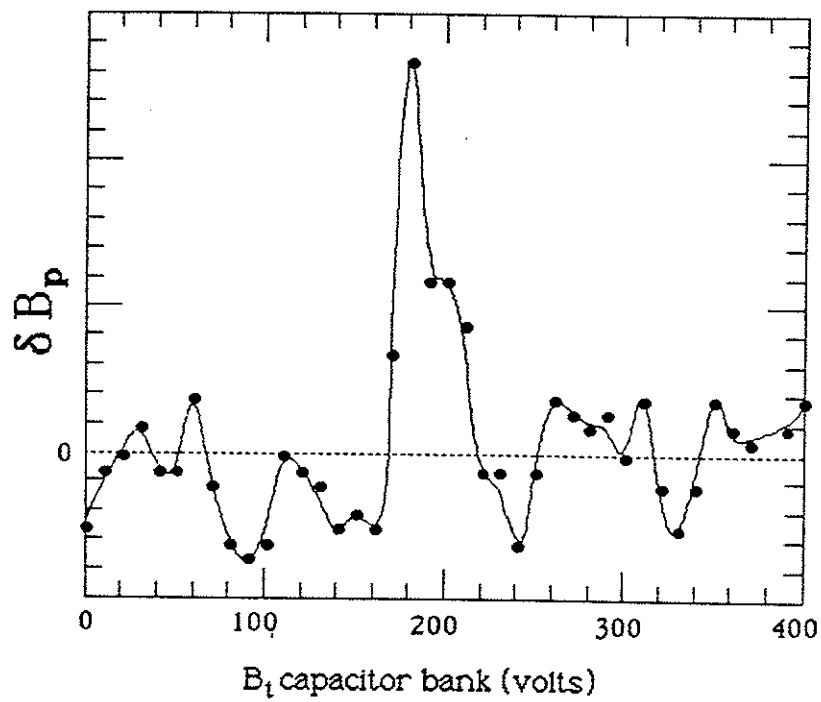

Fig. 4-19. Signal on a magnetic probe as B_t is scanned. $\psi = 7.0$, $t = 0.5$ msec after plasma injection.

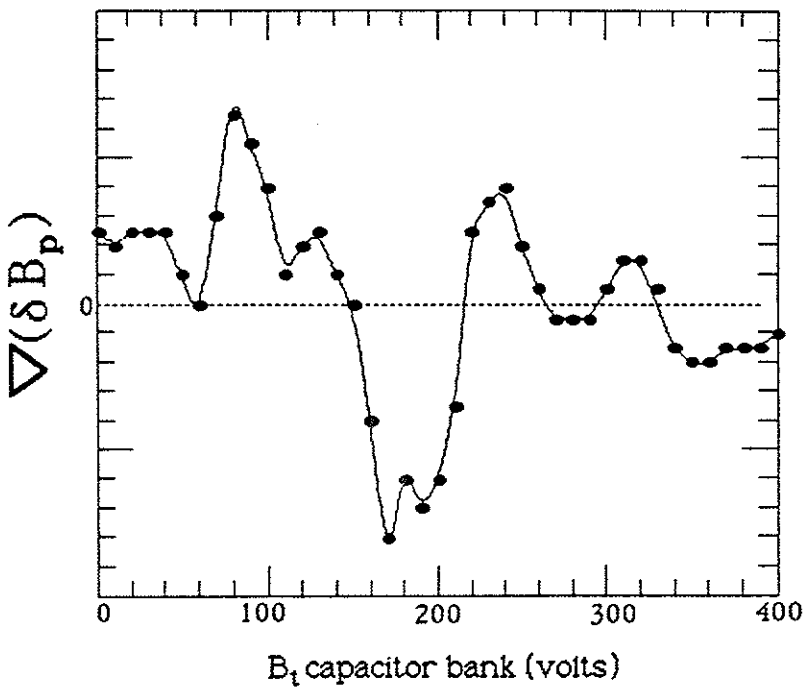

Fig. 4-20. Difference signal from parallel magnetic probes as B_t is scanned. $\phi=7.0$, $t=0.5$ msec.

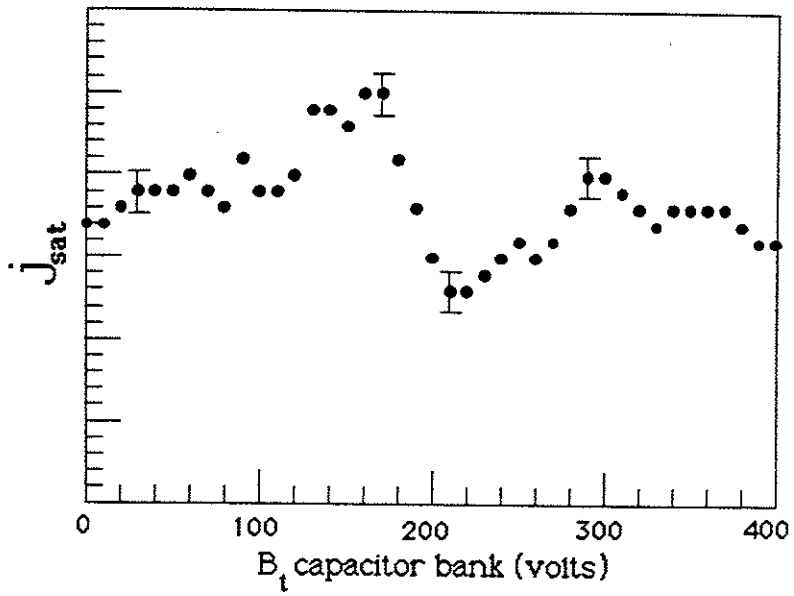

Fig. 4-21. The ion saturation current, to a Langmuir double tipped probe, exhibits a sharp dip as the toroidal magnetic field is increased.

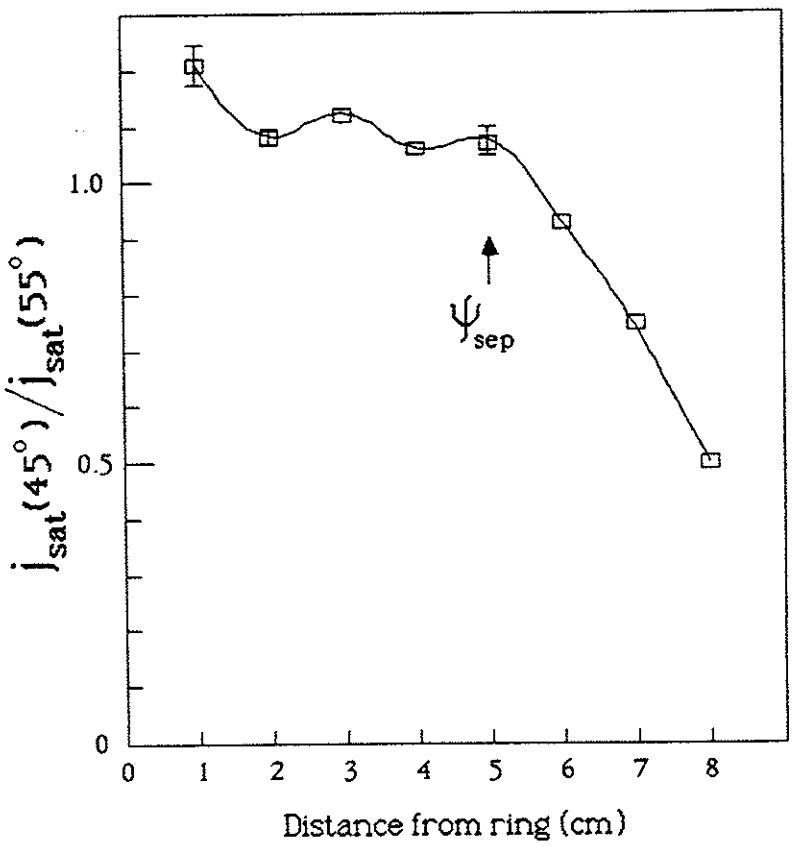

Fig. 4-22. Radial profile of the ratio of ion saturation currents at toroidal angles $\phi = 45°$ and $\phi = 55°$ for the lower outer bridge region, at a ratio of B_t/B_p such that the j_{sat} "dip" is at $\phi = 45°$.

Chapter 5

Conclusions

The measured parallel current density in the Octupole does not fit the theory for neoclassical currents in an axisymmetric torus. In some cases the parallel current is too large or flows in the wrong direction. The parallel current should approach zero with the pressure gradient, which it does not do. In all these measurements the perpendicular current density has the expected magnitude and time decay, which lends a degree of confidence to the methods used to measure the currents.

There are strong indications that either field errors or anomalous gradients in the pressure on a flux surface are affecting the current flow in the common flux region. The anomalous values of magnetic field and ion saturation cur-

rent, measured as $\vec{B}_t$ was scanned, indicate that for the common flux region the axisymmetric theory may be invalid. It is not clear if the lesser asymmetries in the private flux region might affect the currents there also. Certainly the assumption, that quantities such as pressure and temperature are constant on an axisymmetric flux surface, cannot be true. Theoretical predictions[36] indicate that nonaxisymmetry leads to a lessened neoclassical current, so perhaps pressure gradients along a flux surface are a more important effect in the Octupole. Since specific details of the field errors are unknown, no attempts have been made to amend the theory to account for the field errors.

Details of the diffusion process in the Octupole, for the range of plasma parameters used in this experiment, are not well known. There is evidence that transport in the common flux region may be enhanced over the transport in the regions of private flux[17]. The inward movement of the pressure profile has been linked to the difference in transport between these two regions. In some cases the transport in the common flux region can be explained by invoking vortex diffusion processes [17] while diffusion in the private flux scaled classically. Since existence of the parallel bootstrap current is intimately related to the diffusion process, through the neoclassical transport theory, it may not be unreasonable to expect a divergence of the parallel current from

the predicted neoclassical values in a plasma that doesn't exhibit neoclassical diffusion.

Other investigations[12] have concluded that the parallel current in the private flux regions fits the predicted bootstrap values. The disparity, between those results and the conclusions reached in this investigation, is rooted in differences in analysis and data taking techniques. Since the Octupole program was phased out to facilitate ongoing reversed field pinch experiments we were unable to repeat the Octupole bootstrap experiments and resolve the disparity.

One point that can definitely be made is that magnetic field errors can be insidious in their ability to confound experiments dependent on error free axisymmetric fields. With this lesson in mind much effort has gone into the elimination of field errors from the new Madison Symmetric Torus, which is a reversed field pinch device and sensitive to field errors.

In all, comparison of the experimental data with the neoclassical theory is inconclusive. At this point it is not possible to determine if the viscous forces generate bootstrap current in the Octupole or if other processes might be generating currents that mask the bootstrap current.

Bibliography

[1] A.A. Galeev, and R.Z. Sagdeev, *Sov. Phys.-JETP* **26**, 233 (1968).

[2] F.L. Hinton, and R.D. Hazeltine, *Rev. of Mod. Phys.* **48**, 239 (1976).

[3] A.A. Galeev, *Sov. Phys.-JETP* **32**, 752 (1971).

[4] R.J. Bickerton, J.W. Connor, and J.B. Taylor, *Nat. Phys. Sci.* **229**, 110 (1971).

[5] S.P. Hirshman, and D.J. Sigmar, *Nucl. Fusion* **21**, 1079 (1981).

[6] R.A.E. Bolton, J. Hugill, D.J. Lees, W. Miller, and P. Reynolds, *Plasma Physics and Controlled Nuclear Fusion Research, Vol. III*, IAEA, Vienna(1971) 79.

[7] M.S. Berezhetsky, S.E. Grebentshikov, I.S. Sbitnikova, and I.C. Shpigel, *Plasma Physics and Controlled Nuclear Fusion Research, Vol. III*, IAEA,

Vienna(1971) 49.

[8] A.G. Dikii, Yu.K. Kuznetsov, V.K. Pashnev, and V.M. Tonkopryad, *Sov. J. Plasma Phys.* **3**, 2 (1977).

[9] J.T. Hogan, *Nuclear Fusion* 21, 365 (1981).

[10] J.D. Treffert, J.L. Shohet, and H.L. Berk, *Phys. Rev. Lett.* **53**, 2409 (1984).

[11] M.C. Zarnstorf, *28th Annual Meeting of the Division of Plasma Physics*, Baltimore 1986 (APS) Paper 1I2.

[12] M.C. Zarnstorff, Ph.D. Thesis, Physics Dept., University of Wisconsin, Madison, Wi. (1984).

[13] M.C. Zarnstorff and S.C. Prager, em Phys. Rev. Lett. **53**, 454 (1984).

[14] M.C. Zarnstorff and S.C. Prager, *Phys. Fluids* **29**, 298 (1986).

[15] H.R. Garner, Ph.D. Thesis, Nucl. Engr. Dept., University of Wisconsin, Madison, Wi. (1983).

[16] J.C. Sprott,*Rev. Sci. Instr.* **39**, 1569 (1968).

[17] A.G. Kellman, Ph.D. Thesis, Physics Dept., University of Wisconsin, Madison, Wi. (1983).

[18] S.I. Braginski, "Transport Processes in a Plasma", *Reviews of Plasma Physics*, Vol. 1 (Consultants Bureau, New York, 1965), p. 205.

[19] B.B. Robinson, and I.B. Bernstein, *Ann. Phys.* **18**, 110 (1962).

[20] S.P. Hirshman, and A.H. Boozer, PPPL-1409, Princeton Plasma Physics Laboratory, Princeton, NJ (Dec 1976).

[21] S.P. Hirshman, *Phys. Fluids* **21**, 224 (1978).

[22] R.D. Hazeltine, *Plasma Physics* **15**, 77 (1973).

[23] P.H. Rutherford, *Phys. Fluids* **13**, 482 (1970).

[24] M. Abramowitz and I.A. Stegun, *Handbook of Mathmatical Functions*, National Bureau of Standards, USGPO, Washington, D.C. (1964).

[25] G.F. Chew, M.L. Goldberger and F.E. Low, *Proc. R. Soc. London* **236**, 112 (1956).

[26] K.C. Shaing and J.D. Callen,*Phys. Fluids* **26**, 617 (1983).

[27] H.K. Meier, S.P. Hirshman, D.J. Sigmar, and L.L. Lao, ORNL/TM-7584, Oak Ridge National Laboratory, Oak Ridge, Tn. (March 1981).

[28] S.P. Hirshman and D.J. Sigmar, *Phys. Fluids* **20**, 418 (1977).

[29] K.C. Shaing and J.D. Callen, *Phys. Fluids* **26**, 1526 (1983).

[30] F.L. Hinton and M.N. Rosenbluth, *Phys. Fluids* **16**, 836 (1973).

[31] S.P. Hirshman, D.J. Sigmar, and J.F. Clarke, *Phys. Fluids* **19**, 656 (1976).

[32] R.L. Willig, Report PLP 471, Physics Dept., University of Wisconsin, Madison, Wi. (1972).

[33] D.C. Morin, Report PLP 523, Physics Dept., University of Wisconsin, Madison, Wi. (1973).

[34] J.F. Etzweiler and D.A. Brouchous, *Phys. Fluids* **23**, 2447 (1980).

[35] D.J. Holly, Ph.D. Thesis, Physics Dept., University of Wisconsin, Madison, Wi. (1982).

[36] K.C. Shaing and J.D. Callen, *Phys. Fluids* **26**, 3315 (1983).

[37] J.R. Drake, Report PLP 537, Physics Dept., University of Wisconsin, Madison, Wi. (1973).

This research was supported by the U.S. Department of Energy.